Flame dynamics of a subscale rocket combustor operating with gaseous methane and gaseous, subcritical or transcritical oxygen

Stéphane Boulal, Nicolas Fdida, Matuszewski Lionel, Lucien Vingert, Miguel Martin-Benito

Flame Dynamics of a Subscale Rocket Combustor Operating with Gaseous Methane and Gaseous, Subcritical or Transcritical Oxygen

Stéphane Boulal[a,*], Nicolas Fdida[a], Lionel Matuszewski[a], Lucien Vingert[a], Miguel Martin-Benito[b]

[a] *DMPE, ONERA, Université Paris Saclay, F-91123 Palaiseau, France*
[b] *CNES, Launchers Directorate, Paris, France*

Abstract

This article describes an experimental investigation into the flame dynamics of a subscale rocket combustor operating with five shear-coaxial injectors fed with methane and oxygen. We describe three cases labeled after the thermodynamic state at which oxygen is injected into the combustor: gaseous, subcritical or transcritical, whereas methane is continuously injected at a gaseous state. We employ the backlit and OH* chemiluminescence imaging techniques to describe the oxygen atomization and flame dynamics. We provide, with high time-resolution, visualizations of the transitional dynamics of the oxygen injection across the saturation line and through the critical pressure. The Gaseous Case presents a Low-Frequency instability which manifests by an apparent flapping of the flame. The instability is analyzed by means of the Spectral Proper Orthogonal Decomposition technique to reveal the space/time coherence of the instability. It appears that the instability could lock itself inside the combustor as a result of a coupling mechanism between the 1L acoustic resonance of the oxygen feed line and a confinement-induced hydrodynamic instability of the combustion chamber. We observe another flapping instability when the oxygen is in the liquid state (Subcritical and Transcritical cases). This apparent self-induced instability seems to occur at a constant Strouhal number of St = 0.051. Finally, we provide quantitative descriptions of the atomization process in terms of (i) the dynamic evolution of the liquid core length and (ii) a probabilistic characterization of the oxygen spray.

Keywords: Liquid Rocket Engine, Methane oxy-combustion, Liquid oxygen, Atomization, Low-Frequency Instability, Spectral Proper Orthogonal Decomposition

1. Introduction

In the frame of ESA Future Launchers Preparatory Program (FLPP), a new generation of engines propelled by liquid oxygen (LOx) and methane (CH_4) for reusable launchers is under study with the Prometheus demonstrator development. The use of LOx/CH_4 in future combustion devices brings new specific challenges for European Liquid Propulsion R&D programs. Part of these challenges are tackled within the common CNES/ONERA C3PO (*Combustion Cryotechnique CH4 plus Oxygène*) program. Despite a reduction of around ten percent of specific impulse relative to that of hydrogen, the use of methane is motivated by its advantageous physical properties, e.g., higher density (six times that of hydrogen), higher boiling temperature (closer to that of oxygen), lower molecular diffusivity (less prone to leakage), lower susceptibility to detonation initiation, no embrittlement of metal-alloy casings, no particular coking concerns (as opposed to kerosene) and no toxicity issues (as opposed to hydrazine derivatives). As such, the choice of methane in a Liquid Rocket Engine (LRE) allows for simpler and lighter design, easier storability and handling, reduced development and production costs, all of which make methane a strong fuel candidate for reusable operations. However, compared to hydrogen oxy-combustion, methane oxy-combustion involves new challenges, which must be addressed, e.g., less reliable ignition, soot-induced radiative heat load and line clogging. On the negative side, because of the organic nature of the methane molecule, combustion products contain carbon dioxide (CO_2) and soots, which are detrimental for the environment, especially in the context of an increasing popularisation of commercial spaceflights.

Although the definition of combustion chambers operating with this new combination of propellants will ultimately rely on extensive test campaigns, the industry can benefit from computational tools, limiting the number of iterations before reaching a consolidated design. Numerical simulations of the combustion occurring within LREs have to cover a wide range of intricate processes. These are, for example, the primary and secondary atomizations, the droplet vaporization, the reactants mixing and turbulent combustion. Such complexity implies that numerical simulations of LREs remain hardly predictive and require long computational times. Besides, they still demand validations based on thoroughly instrumented experimental test cases.

In France, among other R&D actors, CNES and ONERA are actively working around the Mascotte test facility towards a better characterization of methane oxy-combustion through experimental investigations, e.g., [1] or numerical simulations, e.g., [2].

A Liquid Rocket Engine operates in a large domain of con-

*Corresponding author
Email address: stephane.boulal@onera.fr (Stéphane Boulal)

ditions [1]. Besides, if the engine is of the gas-generator type, the propellants are burning in different mixture ratio ranges, e.g., fuel-rich in the gas-generator and near-stoichiometric fuel-rich in the main combustion chamber. Also, depending on the engine operation, the thermodynamic phase of the propellants can either be gaseous, liquid (subcritical or transcritical) or supercritical. An in-depth understanding of the combustion behavior is even more significant if reusability – which involves engine throttling – is sought.

The literature dealing with CH_4/O_2 combustion for LRE applications is composed of some key experimental studies, e.g. [3], whereas numerical works have gained increasing attention, e.g., [2, 4, 5]. For over 15 years, The Mascotte testbed has been continuously employed to study methane oxy-combustion phenomena. These are, for example, (i) the flame structure under various combinations of CH_4/O_2 injection regimes [1, 3, 6, 7], (ii) the liquid propellant(s) atomization [8], (iii) the High-Frequency (HF) instabilities [9, 10] or (iv) the heat transfer at the combustion chamber walls [11]. Furthermore, these studies have also been used as validation cases of plentiful numerical works [1, 2, 4, 5, 12–17]. A more exhaustive list of references involving CH_4/O_2 shear-coaxial injection is given in Table 1. The list is sorted in a comprehensive way depending on the propellants' thermodynamic state upon injection.

There is still a need for the qualification of LRE-combustor's transitory phases, whereby the thermodynamic state of the propellants may affect the flame behavior. The present experimental work is motivated by (i) the visualization of the flame and flow dynamics at canonical operating conditions based on the thermodynamic state of the oxygen, namely the gaseous, subcritical and transcritical states and (ii) the analysis of the transition from the gaseous to the subcritical states and from the subcritical to the transcritical states. In Table 1, we highlight the groups of references to which this work can directly compare.

The present article is structured as follows. In Section 2, we describe (i) the Mascotte facility, (ii) the subscale combustion chamber employed, (iii) the optical diagnostics set to image the combustion and liquid jet dynamics, namely OH* chemiluminescence and backlit visualizations and (iv) the operating conditions achieved during the campaign. In Section 3, we present the experimental results. More specifically, we compare cases and their associated transient operations to one another. The transitions from gaseous to liquid and from subcritical to transcritical states are also qualitatively described. In Section 4, we provide four quantitative analyses. The first one relates to a Low-Frequency (LF) instability observed in gaseous conditions. In order to better comprehend this instability, we apply the Spectral Proper Orthogonal Decomposition (SPOD) technique to the OH* chemiluminescence recording. The second one describes the unsteady dynamics of the liquid-oxygen jet. SPOD analysis is performed here on the backlit recordings to reveal the underlying mechanisms of the jet instability. The last two address the atomization process.

2. Experimental setup

2.1. The Mascotte facility and the Bhp-HrM combustion chamber

Developed at ONERA in the early '90s, the Mascotte facility is a unique test rig (in France) designed to investigate the fundamental aspects of cryogenic combustion [37, 38]. These are, non-exhaustively, the phenomena of ignition, atomization, combustion instabilities or wall heat transfers. As opposed to actual LREs, the bench is highly instrumented with a myriad of sensors (pressure transducers, flowmeters, thermocouples, flux meters). In general, it is fitted with optical accesses allowing for non-intrusive investigations of cryogenic combustion. As such, the aforementioned phenomena can be finely characterized in conditions representative of actual LREs, yet on a much smaller scale and at a significantly lower cost.

The combustion chamber used in this study is specifically designed to run at high pressure and high mixture ratios. It is called *Boitier Haute Pression et Haut Rapport de Mélange* or Bhp-HrM for short and is schematically represented in Figure 1 (a). Share-funded by CNES and ONERA, it has been used in previous test campaigns [11, 39–41] and is numerically simulated in [42]. It consists of a 615-mm long horizontal tube composed of interchangeable modules of 56-mm circular cross-section. The propellants, i.e., the oxygen and the methane, are

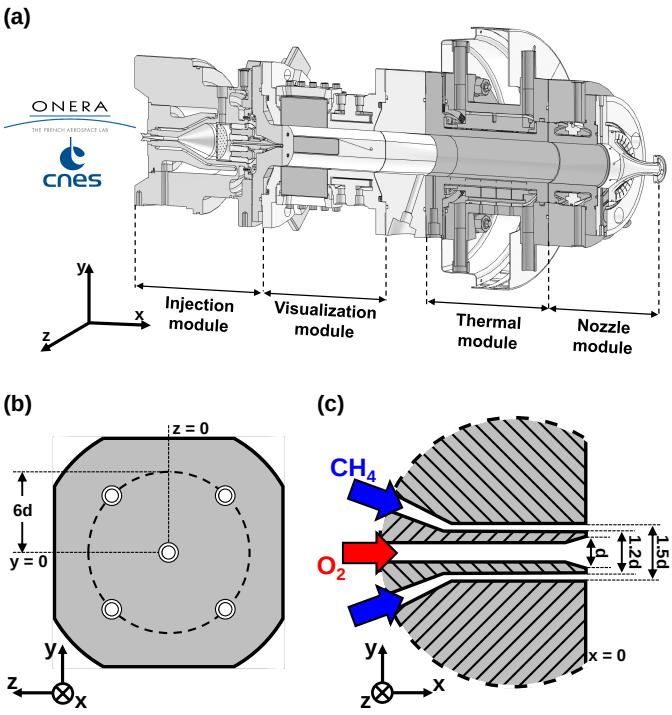

Figure 1: **(a)** Three-dimensional view of the Bhp-HrM combustion chamber. Non-pertinent elements have been stripped off from the digital mock-up. **(b)** Schematic front view of the injection plate showing the five shear-coaxial injectors. **(c)** Schematic cross-sectional view of a single injector element.

fed to the chamber through five shear-coaxial injectors mounted with no recess in an "X" arrangement, i.e., with a central injector located at the center of a circle whereby the four others are

Methane CH_4 \ Oxygen O_2	Gaseous	Subcritical	Transcritical
Gaseous	● [11, 18–25]	● [2, 6–11, 26–32]	/
Subcritical	/	[1, 33]	/
Transcritical	/	[33]	[1, 3, 5, 33]
Supercritical	/	● [3, 6, 11, 27, 31, 32]	● [3, 4, 6, 10–17, 27, 31, 32, 34–36]

Table 1: Literature survey of CH_4/O_2-based combustion studies sorted according to the thermodynamic state of both propellants. Only the studies relative to shear-coaxial injection are listed. The operating regimes achieved during the test campaign of the present work are highlighted in colored circles.

symmetrically positioned. A shear-coaxial injector consists of two concentric tubes whose inner and outer parts are respectively fed with oxygen and methane. Figure 1 (b, c) provides schematics views of the injection plate and of a shear-coaxial injector. The inner tube diameter is noted d and will be used in the following for all non-dimensionalizations. The inner and outer diameters of the methane annulus are, respectively, $1.2d$ and $1.5d$.

Each propellant is fed from a pressurized vessel where it is stored in gaseous or liquid form. For the oxygen, the injection circuit is jacket-cooled (from the liquefied tank down to a position just upstream of the injection plate) by means of liquid nitrogen (N_2) so as to ensure the fluid remains in liquid form. In this work, methane of purity $> 99\%$ is consistently injected in the gaseous state at ambient temperature, and oxygen is either injected in the gaseous state at ambient temperature or in the liquid state at a temperature of ~ 100 K (see §2.3).

A visualization module is placed just downstream of the injection plate ($x = 0$ plane). This module can be equipped with up to four optical ports to allow for the imaging of the combustion dynamics. In the present configuration, this is realized (see §2.2) by means of two lateral 40-mm-thick quartz visualization windows mounted on opposed optical ports. Their inner faces are film-cooled by injecting a helium (He) layer through the slit formed at the interface between the injection and visualization modules. In general, the helium film-cooling mass flow is set to between five and ten percent of the total mass flow. From the combustion-chemistry viewpoint, helium does not affect the behavior of the flames since it is chemically inert. The bottom port is equipped with a plain flange fitted with thermocouples. The top port consists of a flange whereby an ignition torch (not represented in Figure 1) is mounted to establish the combustion in the chamber. The torch comprises a small pilot chamber, which is fed with gaseous hydrogen and gaseous oxygen. The mixture is spark-ignited, and the resulting jet flame directs towards the main CH_4/O_2 jets at a 90° angle. Although being symmetric, the cross-section of the visualization module is not strictly circular as it presents four planar edges required for the optical ports. A thermal measurement module is located downstream of the visualization module. It is equipped with various thermocouples to characterize the wall heat transfers. We will not present those measurements here, but a thorough characterization in a similar configuration and at various operating conditions can otherwise be found in [11]. An interface module ensures the smooth transition from the nearly circular cross-section of the visualization module towards the circular cross-section of the thermal measurements module. At the back-end, a converging nozzle completes the assembly. Each module is water-cooled in order to sustain the harsh environment within the combustion chamber.

2.2. *Dual high-speed visualizations*

Two simultaneous visualization techniques have been employed. These are the backlit and the OH* chemiluminescence imaging techniques, schematically represented in Figure 2. Each technique has been previously employed on a number of LREs-targeted studies, either conjointly [1, 6, 8, 10, 26–30, 40, 43–46] and/or in combination with CH* chemiluminescence [3, 9, 10, 24, 31] or OH-PLIF [7, 28, 47–49] techniques.

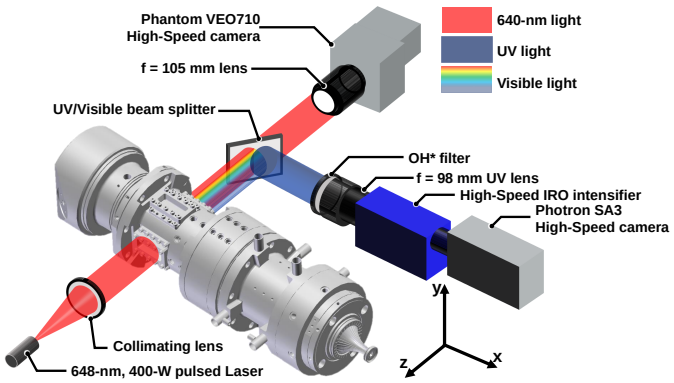

Figure 2: Schematic view of the dual high-speed visualization setup.

Backlit imaging consists of visualizing the shades formed by the dense liquid phase upon irradiance from a collimated beam. Note that the shadowgraphy technique has also significantly been applied to study the liquid-oxygen atomization in reacting conditions [37, 50–52]. For large density gradients, such as those encountered in shear-coaxial injectors, backlit and shadowgraphy techniques essentially return the same qualitative information. Here, the backlit effect is created employing a Cavilux Smart 400-W laser, which emits pulsed incoherent monochromatic light of 648 ± 10 nm-wavelength. On the opposite side of the visualization module, a beam splitter separates the light - comprising that coming from the laser source and that emitted by the combustion - into a transmitted component in the visible range and a reflected component in the Ultraviolet (UV) range. The latter is used for the OH* chemiluminescence imaging (see below). The transmitted visible component is focused towards a Phantom VEO710 High-Speed camera through a $f = 105$-mm-lens (f/5.6). The camera is equipped with a CMOS sensor providing a 1280×800

pixels-image-definition encoded on 12 bits, i.e., 4096 Digital Levels (DL). The camera/lens combination provides a field of view covering the whole visualization window, with a resolution of 96 µm/pixel. The camera is set to the 1-µs-minimum exposure time to limit the amount of flame emission collected. The laser pulse duration – set to 40 ns – controls the exposure. It acts as a shutter by kinetically freezing the flow's liquid region, ensuring satisfactory time resolution.

OH* chemiluminescence imaging consists of visualizing the excited hydroxyl radical (OH*) produced by the combustion chemical reactions. Spontaneous emission of OH* occurs in the near UV between 300 and 325 nm [1, 31, 43, 52–54]. As opposed to the OH-PLIF technique [7, 28, 47–49], which images the fluorescence signal of the OH species (including that at equilibrium), OH* chemiluminescence is commonly accepted to be an adequate tracer of the heat release locations [54–56], i.e., that of the flame fronts. OH* chemiluminescence is favored over that of CH* because it has been shown to provide a better signal-to-noise ratio [9, 31], particularly at high pressure [1]. OH* chemiluminescence imaging is line-of-sight integrated. Hence, it does not constitute a spatially-resolved quantity, as opposed to OH-PLIF. In [54], the authors tried to correlate the heat release and the OH* chemiluminescence recording of a lean, partially premixed, swirled flame. Based on Abel-deconvoluted fields, the proposed methodology requires knowledge of the average strain rate of the imaged flow and has not been proven to work for non-premixed flames. For those, another method of heat release evaluation is proposed in [57] but remains limited to the case of laminar diffusion flame. In this work, we limit the analysis of the OH* chemiluminescence to the raw data recorded.

In practice, OH* chemiluminescence is imaged as follows. The OH* emission is spectrally selected – from the reflected UV beam (see Figure 2) – through a narrow-band filter of 310 nm-central wavelength, 10-nm-FWHM and 70-percent-maximum transmission. A Photron Fastcam SA3 High-Speed camera coupled to a Lavision HS-IRO image-intensifier then collects the OH* signal. The intensifier is used to capture the UV signal and to render it suitable for the camera. The gate-opening time of the intensifier – set to 700 ns – controls the exposure. The camera is equipped with a 12-bits-ADC sensor, which provides a 1024×512 pixels-image-definition, with an exposure time of 2 µs. A f = 98-mm-UV lens (f/8) is mounted on the intensified camera allowing a 80 µm/pixel-image-resolution.

Both cameras operate at an acquisition rate of 1 kHz, allowing a recording duration of approximately 10 s. They are time-synchronized, and their fields of view are carefully adjusted to match one another. Since the goal of the present work is to record transitional dynamics, we favor long-duration recording over the acquisition rate. On the backlit imaging, the 1-kHz-acquisition rate is too low to allow for the tracking of individual liquid elements (droplets or ligaments). To overcome this limitation, we performed reruns (see §2.3) and operated the backlit camera at an acquisition rate of 15 kHz. As opposed to previous works [11, 40, 41] performed on the Bhp-HrM combustion chamber, where the four outer injectors were placed in a "+" arrangement along a circle of smaller radius, the present configuration allows the complete visualization (in the y direction) of the central-injector flame, limiting that of surrounding ones.

In parallel with the two high-speed visualizations, we employ a conventional video camera (not represented in Figure 2) to image the combustion chamber at a 25-Hz-frame-rate and a 100-µs-exposure-time. It monitors the rig operation in real-time and provides a complementary three-dimensional insight into the combustor.

2.3. Operating conditions

During the test campaign reported in this work, we achieved three operating conditions. They are labeled after the thermodynamic state attained by the oxygen injection. These are the Gaseous Case, the Subcritical Case and the Transcritical Case. For the latter, there is no consensus in the literature as to whether this state should be called transcritical or supercritical [58]. Although in [58], the authors have proposed that the only frontier, which should exist in the Pressure-Temperature diagram, is that joining the saturation and the pseudo-boiling lines, we retain the transcritical labeling convention introduced in [51], considering that the supercritical state is, by strict thermodynamic definition, only achieved when both the fluid pressure and temperature are above critical values (P_c^{O2} = 5.042 MPa, T_c^{O2} = 154.5 K). In our study, the oxygen injection temperature remained below its critical value, which justifies the labeling convention. Table 2 gives the experimental conditions of the three cases reported in the study. The indicated values represent the time-averaged quantities reached during the stabilized plateau, characterized by quasi-steady values only varying to within one percent of the mean. On average, this lasted for ~ 5 s, except for the Gaseous Case, which lasted ~ 8 s. Figure 3 gives the trajectory of the Transcritical Case run in the Pressure-Temperature diagram. The oxygen density is computed for illustrative purposes, assuming a Peng-Robinson Equation of State [59]. On top of the thermodynamic conditions, Table 2

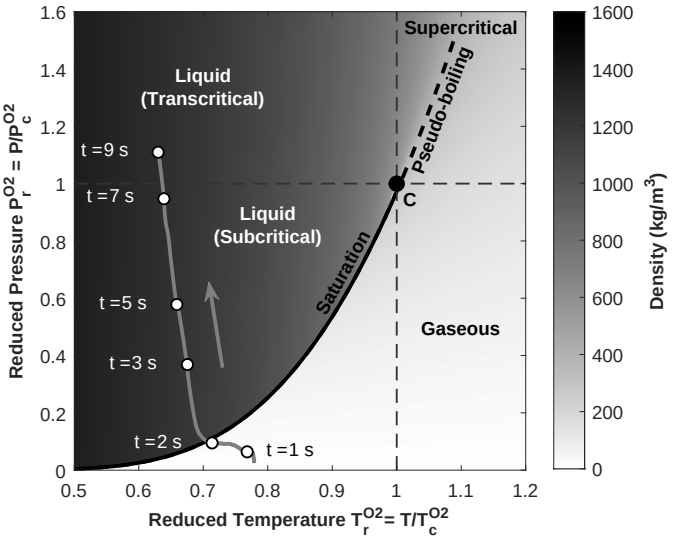

Figure 3: Trajectory (gray line) of the **Transcritical Case** in the Pressure-Temperature diagram of oxygen. The oxygen density is determined assuming a Peng-Robinson Equation of State.

Case	P (MPa)	$T_{\text{inj.}}^{\text{O2}}$ (K)	MR	ϕ	VR	J	We	Re
● **Gaseous**	4.42	290	2.29	1.75	0.96	0.5	n/a	3.7×10^5
● **Subcritical**	4.38	93	2.25	1.78	19.7	9.9	1.1×10^4	4.0×10^4
● **Transcritical**	5.77	95	2.27	1.76	15.1	7.5	1.7×10^4	5.9×10^4

Table 2: Experimental conditions (plateau-averaged values) of the cases reported, P: combustion chamber pressure, $T_{\text{inj.}}^{\text{O2}}$: O_2 injection temperature, **MR**: Mixture Ratio, ϕ: Global Equivalence Ratio, **VR**: Velocity Ratio, J: Momentum Flux Ratio, **We**: Aerodynamic Weber number, **Re**: O_2-injection-based Reynolds number.

also provides the values of the non-dimensional numbers classically used to characterize the injection conditions and atomization regime of shear-coaxial injectors [60–62]. These are:

(i) the Mixture Ratio MR $= \dot{m_{O2}}/\dot{m_{CH4}}$, with $\dot{m_{O2}}$ and $\dot{m_{CH4}}$ the O_2 and CH_4 mass flows. For reference, the values of the global Equivalence Ratio $\phi = \text{MR}_{\text{st}}/\text{MR}$, where $\text{MR}_{\text{st}} = 4$ is the stoichiometric mixture ratio, are also given.

(ii) the Velocity Ratio VR $= U_{CH4}/U_{O2}$, with U_{O2} and U_{CH4} the O_2 and CH_4 injection velocities.

(iii) the Momentum Flux Ratio $J = \rho_{CH4} U_{CH4}^2 / \rho_{O2} U_{O2}^2$, with ρ_{O2} and ρ_{CH4} the O_2 and CH_4 densities.

(iv) the aerodynamic Weber number We $= \rho_{CH4} U_{CH4}^2 d/\sigma_{O2}$, with σ_{O2} the O_2 surface tension.

(v) the O_2 flow-based Reynolds number Re $= \rho_{O2} U_{O2} d/\mu_{O2}$, with μ_{O2} the O_2 dynamic viscosity.

Throughout this work, tabulated values from the NIST database [63] are used to obtain the thermophysical properties of each propellant.

For each case, we conducted a non-reactive run, i.e., without operating the ignition torch. For the sake of conciseness, we choose not to present the exploitable visualizations, i.e., the backlit recordings of the Subcritical and Transcritical cases. In addition, we conducted at least two repetitions of the same case. For the Transcritical Case rerun, we operated the recording of the backlit camera at the 15-kHz-acquisition rate. The methane is continuously injected at room temperature in the gaseous state, except for the Transcritical Case, which achieved a strict supercritical state with both pressure and temperature stabilizing above the methane critical values ($P_c^{CH4} = 4.599$ MPa, $T_c^{CH4} = 190.6$ K). For all the cases considered, the stabilized-plateau value of the Mixture Ratio is at a relatively constant value of MR ≈ 2.3. This will ease the comparisons between cases described in §3.1, at least within stabilized plateaux. According to the classification of shear-coaxial atomization regimes proposed in [60], fiber-type atomization is expected. It is characterized by the production of thin and short liquid fibers peeling off from the liquid-core periphery as soon as the liquid jet exits the nozzle [64].

Figure 4 qualitatively compares visualizations of the combustor (in true colors), as imaged by the conventional video camera, for conditions of gaseous, subcritical and transcritical oxygen-injection.

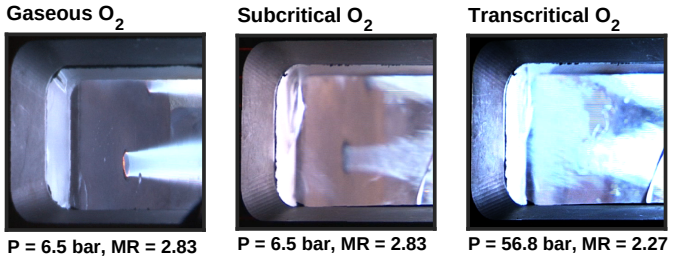

Figure 4: True-colors visualizations of the combustor for conditions of **gaseous** (left), **subcritical** (middle) and **transcritical** (right) oxygen injection.

3. Results

3.1. Cases descriptions and comparisons

For the three cases, Figure 5 shows the evolution of the pressure P within the combustion chamber. For the Subcritical and Transcritical cases, the evolution of the oxygen saturation pressure $P_{\text{sat}}^{\text{O2}}$ is also plotted. Ramping-ups of the pressure are achieved in two stages. The torch operates between $t = -0.4$ s and $t = 2$ s. The recording triggers at $t = 0$ s. Stabilized plateau is achieved at $t \approx 7$ s for the Gaseous Case and $t \approx 10$ s for the Subcritical and Transcritical cases. This difference is due to the longer time required to stabilize the liquid-oxygen mass flow. Two characteristic times t_1 and t_2 are shown in Figure 5. The first one is the time at which the chamber pressure exceeds the oxygen-saturation pressure, i.e., when the condensation of the oxygen begins. The second one is the time at which the chamber pressure reaches the oxygen critical pressure. We will use these times to locate and portray the two transitions described in detail in §3.2 and §3.3. As opposed to previous works [27, 44], Low-Frequency (LF), high-amplitude pressure oscillations are not observed within the combustion chamber.

Figure 6 shows instantaneous images from both high-speed recordings of the three studied cases, taken within their respective stabilized plateaux. The ($x = 0$) plane and the ($y = 0$) axis are, respectively, the injection plane and the central-injector axis. The OH* chemiluminescence intensity is represented in false colors and, for each case, the intensity is normalized by its maximum to provide higher contrast. All the cases resulted in the flame anchoring at the injector lip, as observed on the OH* chemiluminescence visualizations. This can also be observed on the true-colors visualizations of Figure 4. Flame closure always occurs downstream of the visualization zone, and we could therefore not ascertain its position. As one might expect, the backlit imaging recorded for the Gaseous Case does not return any useful information. We notice some water droplets

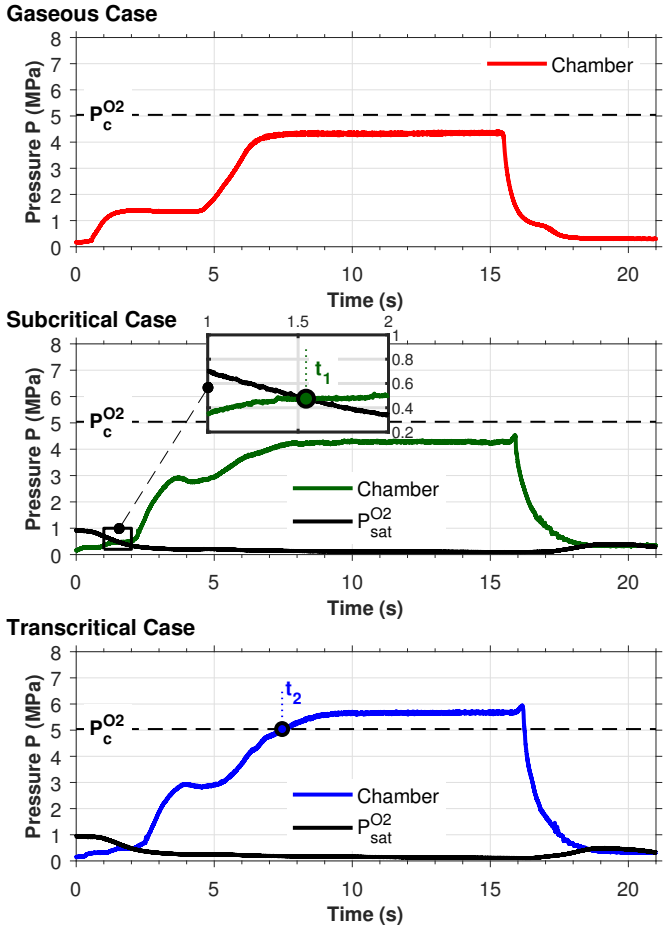

Figure 5: Evolution of the pressure in the combustion chamber for the **Gaseous** (top), **Subcritical** (middle) and **Transcritical** (bottom) cases. P_c^{O2}: oxygen critical pressure. P_{sat}^{O2}: oxygen saturation pressure.

condensing at the windows. The OH* chemiluminescence image shows an off-axis central flame and part of the bottom surrounding one(s). The deviation of the flame from the injector axis is actually due to a Low-Frequency instability locked inside the combustion chamber, which we further analyze in §4.1.

The Subcritical Case resulted in a crack of the foreground visualization window. It is partially tarnishing both visualizations for $6 < x/d < 12$. The backlit visualization shows a dark-horizontal central region corresponding to the liquid-oxygen jet core. It is surrounded by the gaseous methane jet, which is observable at upstream positions ($0 < x/d < 3$) because of its high density. The OH* chemiluminescence image shows an intense heat release zone located in the second half of the visualized zone. This is due to the delay imposed by the processes of atomization, vaporization and mixing. The flame radial extent, i.e., the angle of its cone, is larger in the Subcritical Case than in the Gaseous Case. This is due to oxygen droplets pulling out from the central region, which expands the combustion locations in the radial direction.

For the Transcritical Case, we switched the background and foreground windows to obtain images that are less tainted by the crack. This is why the crack no longer appears on the OH* chemiluminescence visualization. On the backlit visualization, the interface of the liquid-oxygen core is not as sharp as that observed for the Subcritical Case. The intense region of OH* emission has progressed upstream as a result of the disappearance of the surface tension when the pressure goes supercritical (see §3.3). In addition, the flame cone appears to be wider. This observation is confirmed on the OH* chemiluminescence image since the flames of the bottom injectors are discernible, indicating an expansion of each flame in the radial direction. The dynamics of the transition from subcritical to transcritical regimes are further discussed in §3.3.

In order to complete the characterization of the different flame morphologies, Figure 7 compares the OH* intensity distributions corresponding to the instantaneous images of Figure 6. As opposed to the latter, and in order to provide absolute comparisons between cases, the OH* intensity is not normalized here. The distribution of the Transcritical Case appears to be much broader than the other two, which indicates that heat release occurs for a wider range of compositions.

Figure 8 shows the variation of the OH* chemiluminescence space-averaged intensity as functions of the combustion chamber pressure P. OH* chemiluminescence intensity responds almost linearly to the pressure, but with slope differences between cases. At about $P = 2.8$ MPa, we observe a steep jump of the OH* intensity for the Subcritical and Transcritical cases. This is the heat release response to rapid change in the mixture composition (MR) and atomization condition (J) when the second pressure-ramp is initiated, at $t \approx 4.5$ s (see Figure 5). For the same pressure, the Subcritical and Transcritical cases show higher OH* emission intensities than the Gaseous Case. We attribute this to the fact that the gaseous injection is likely to be more efficient than the two-phase injection at mixing the reactants. As such, the distribution of Equivalence Ratio (or mixture fraction) is broader in the Gaseous Case. Thus, a larger proportion of the reactants will burn at local compositions close to the stoichiometry (global composition is fuel-rich), leading to higher heat release levels. Another explanation comes from the larger opening of the flame cone observed for both the Subcritical and Transcritical cases (see Figure 6). However, the Subcritical Case appears to return between about 50 and 100% lower intensities than the Transcritical Case, at the same pressure. From a qualitative viewpoint, we attribute this to (i) the presence of the window's crack for the Subcritical Case, which reduces by $\sim 10\%$ the amount of emission collected by the camera, and (ii) the build-up of soot deposit on the windows during each run, which is not consistently cleaned-up before the next one. Since those experimental interferences could not be reproduced, quantitative comparison should be prohibited.

3.2. *Oxygen condensation and flame anchoring*

For the Subcritical Case, Figure 9 gives composite images of OH* chemiluminescence and backlit visualizations, which we constructed by snipping both visualizations along the central injector axis. The snapshots are chosen to show the oxygen-jet condensation dynamically. According to Figure 5, this occurs around $t = t_1 = 1.554$ s, which is in agreement with the appearance of the liquid jet in Figure 9, between $t = 1.536$ s

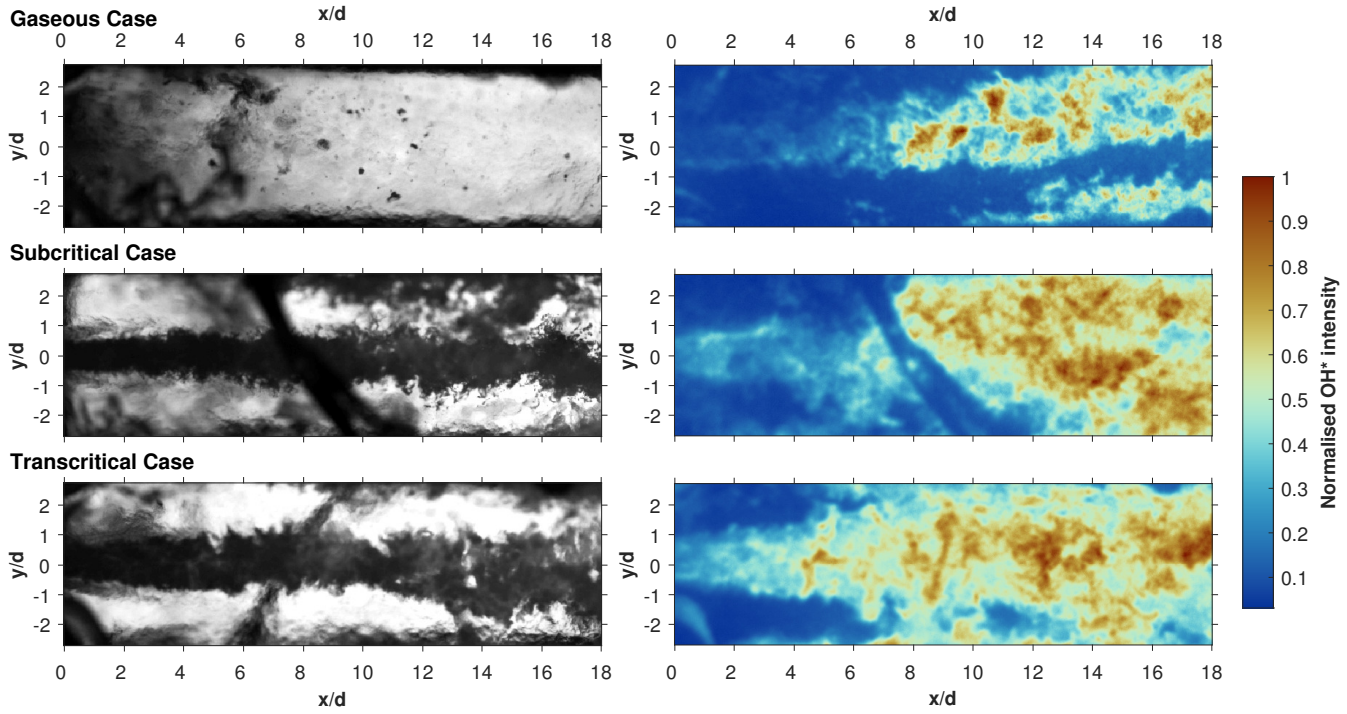

Figure 6: Comparisons of **backlit** (left column) and **OH* chemiluminescence** (right column) instantaneous images (within stabilized plateaux) for the **Gaseous** (top row), **Subcritical** (middle row) and **Transcritical** (bottom row) cases.

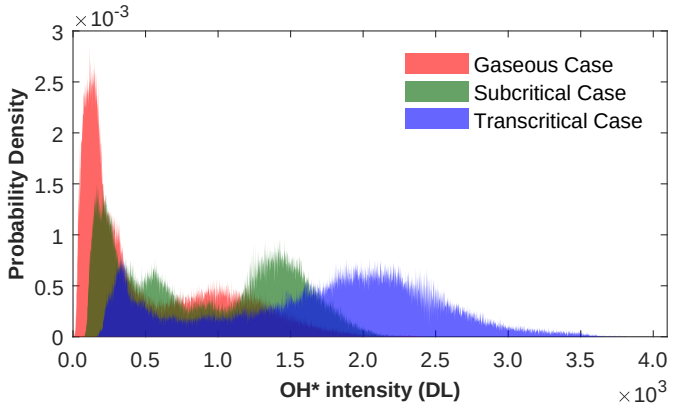

Figure 7: OH* intensity distributions corresponding to the visualizations of Figure 6 obtained within stabilized plateaux.

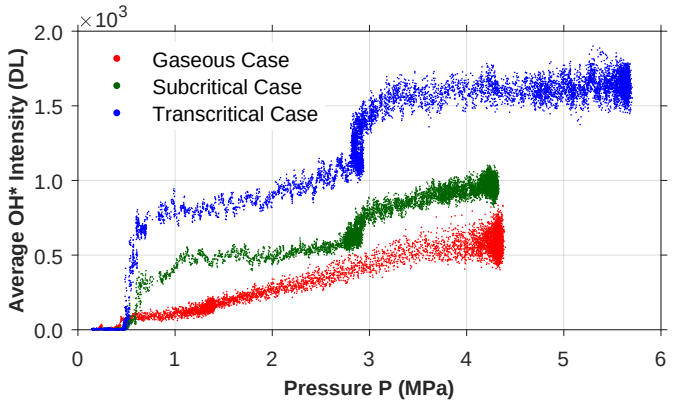

Figure 8: Space-averaged OH* chemiluminescence intensities as functions of the combustion chamber pressure.

and $t = 1.770$ s. On both frames, we note the presence of the GH_2/GO_2 flame flowing from the torch at $x/d \approx 10$.

The oxygen condensation occurs before the flame stabilizes at the injector lip, which is observed on the following frames. The stabilization of the flame results from the rapid deflagration of the premixed reactants present in the outer recirculation zone. In agreement with the mechanism described in [65, 66], the flame front originated from a region ignited by the torch (possibly that surrounding the bottom jets), progressed upstream, reached the injector inner lip and anchored in the vicinity of the oxygen-core boundary in the form of a stable diffusion flame. During this highly transient process, we observe, e.g., at time $t_1 = 2.059$ s, the complete disappearance of the liquid-oxygen core. We understand this to be consecutive to the deflagration propagation, which imposes a pressure close to the injector face plate larger than the oxygen injection pressure, causing the oxygen flow to disrupt temporarily. This pressure peak is, however, not observed on the pressure recording (see Figure 5), presumably because the only pressure tapping within the combustion chamber is located further downstream, at $x/d = 75$. After a period of $\sim$ 10 ms, the liquid-oxygen jet develops again but is now coexistent with the anchored flame.

3.3. Critical pressure crossing

For the Transcritical Case, Figure 10 provides a series of backlit visualizations showing the dynamic evolution of the jet morphology as the oxygen approaches and crosses the transcritical state. The values of the oxygen and methane reduced pressure, $P_r^{O2} = P/P_c^{O2}$ and $P_r^{CH4} = P/P_c^{CH4}$, are also displayed. In addition, we compare, in Figure 11, closed-up views of the liquid interface for, respectively, $P_r^{O2} < 1$ and $P_r^{O2} > 1$.

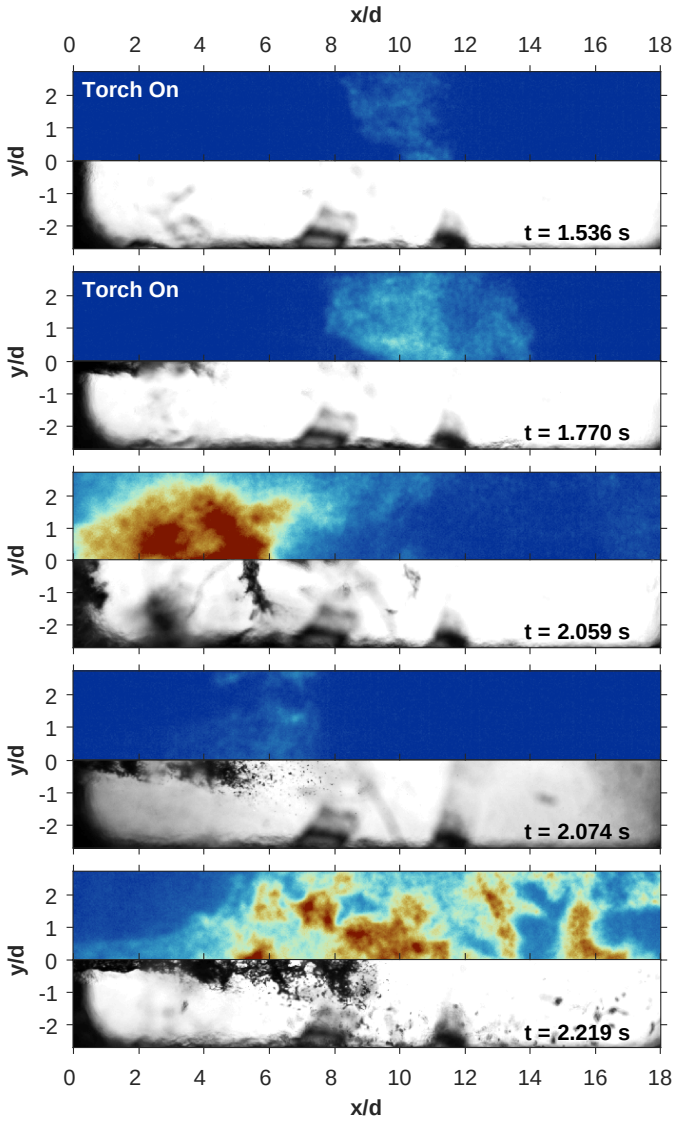

Figure 9: Series of **OH* chemiluminescence** (top) and **backlit** (bottom) composite images of the **Subcritical** Case dynamically showing the oxygen-jet condensation and the flame anchoring at the central injector lip.

For low values of P_r^{O2}, the liquid-oxygen jet features the classical morphology of fiber-type atomization, with ligaments and droplets peeling out from the dense-oxygen core. Along the jet axis, the interface appears to be increasingly corrugated, resulting from the instability developing at the interface. The droplets produced by the primary atomization further reduce in size through vaporization to the surrounding hot gas or through the secondary breakup mechanism, which fragments them into lower-diameter droplets. As the chamber pressure approaches the oxygen-critical pressure, i.e., $P_r^{O2} \rightarrow 1$, we observe the progressive evolution of the liquid-oxygen interface from a sharp and highly corrugated one to a diffuse and smooth one. When the critical pressure is exceeded, a considerably lower number of oxygen lumps (fibers and droplets) detach from the core region. Instead, the liquid-oxygen core appears to get crumbled from the outside. This is explained by the reduction of the liquid surface tension and latent heat of vaporization to near-zero

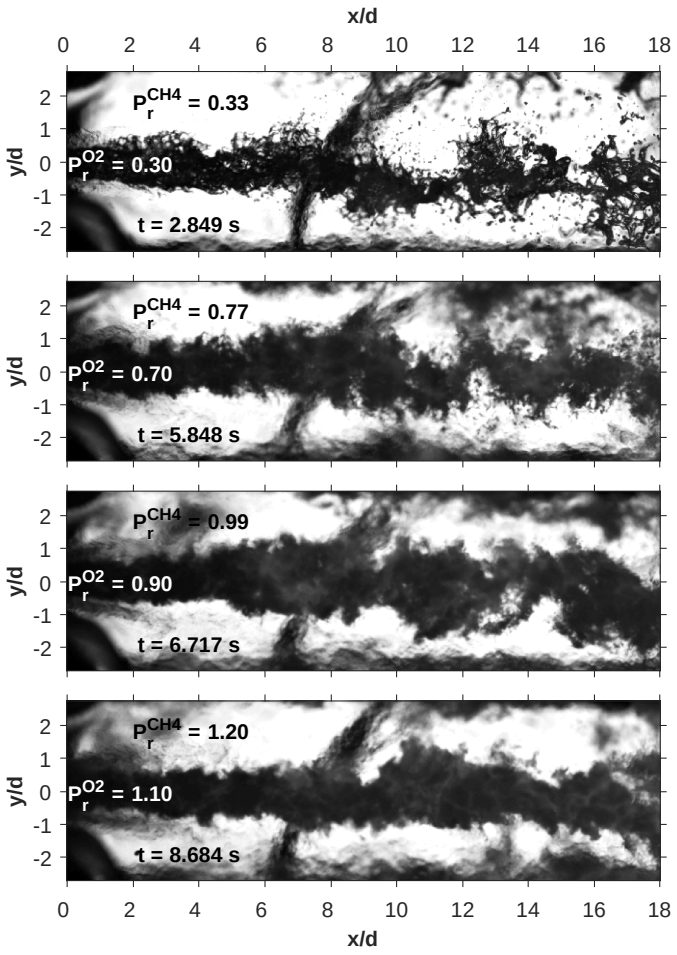

Figure 10: Series of backlit visualizations dynamically showing the evolution of the oxygen from **subcritical** to **transcritical** conditions.

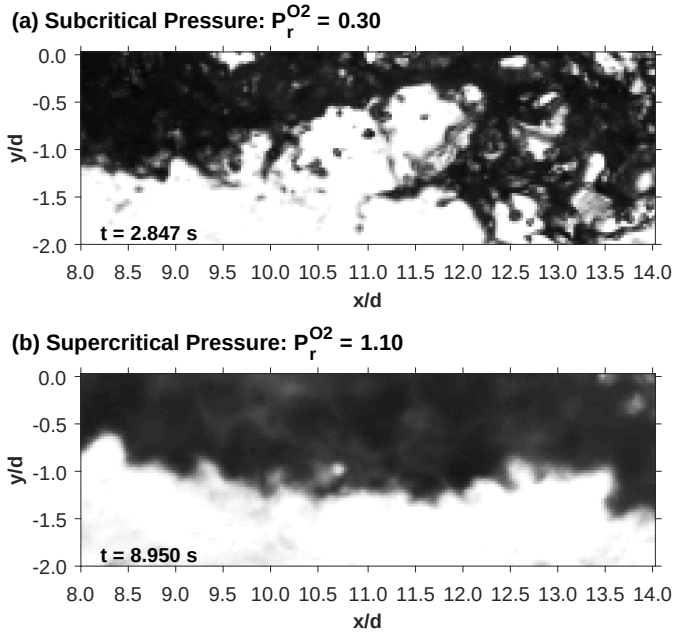

Figure 11: Closed-up views of the liquid-oxygen interface at **subcritical (a)** and **supercritical (b)** pressure.

values as $P_r^{O2} \rightarrow 1$. In such conditions where the surface tension has vanished, the vaporization process is considerably accelerated. We illustrate this point in Figure 12, where we compare the evolutions of single-detached oxygen droplets at subcritical and supercritical pressure. The latter is characterized by non-spherical droplets detaching from the core, which rapidly diffuse, mix and burn with the methane. In fact, the process of vaporization, which characterizes subcritical-type injection, does not exist anymore at supercritical pressure. Instead, it is replaced by the so-called pseudo-boiling, which, phenomenologically, reduces to gas-like diffusion and mixing.

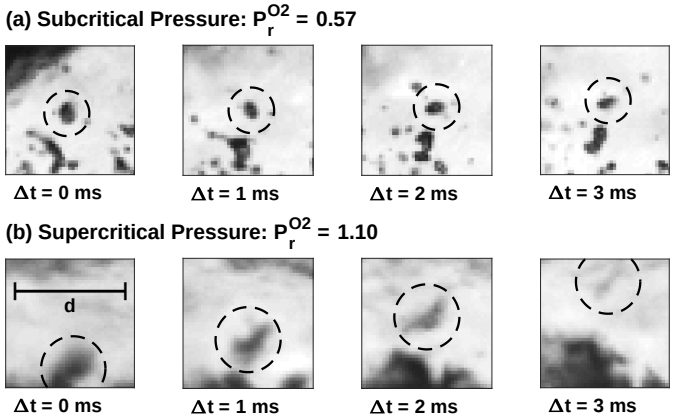

Figure 12: Single-droplet evolution at **subcritical (a)** and **supercritical (b)** pressure. Tracking of the droplets is performed on the 15-kHz-recording of the Transcritical Case 2. The frame of reference is moving with the droplet. Δt: local time frame. d is the injector inner tube diameter.

Simultaneously, as the pressure increases, the methane jet appears to get darker (see Figure 10) as a consequence of an increase in its density. At respectively transcritical and supercritical conditions, the mixing between O_2 and CH_4 resembles more to that found in the shear layer between two turbulent gaseous streams of large density and velocity differences. As a matter of fact, the shapes obtained at the interface recall that of a Kelvin-Helmholtz (KH) hydrodynamic instability. Their dynamics and space/time coherence are further analyzed in §4.2.

In [31], the authors have shown that no phase equilibrium could be achieved for mixtures of O_2 and CH_4 at pressures above $P_r^{O2} = 0.935$. Using the CoolProp package [67] with the thermodynamic data of CH_4/O_2 mixtures from [68], adiabatic-mixing based equilibria between the two component were computed for pressure as high as $P_r^{O2} = 1.079$. However, this numerical result should be put back in perspective considering that (i) adiabatic mixing cannot accurately represent a stretched mixing layer where heat fluxes are expected, (ii) the simplicity of the interaction parameter given in [68] and the scarcity of CH_4/O_2 equilibrium data seems to indicate that the thermodynamic model given in this reference is questionable when it comes to compute CH_4/O_2 equilibria, and (iii) the mixing layers encountered in the operating device are expected to be O_2/combustion products and CH_4/combustion products rather than CH_4/O_2 mixing layers. With the presence of hot combustion products, we did not have visual evidence that the thermodynamic stability of the mixture may have been disrupted by condensing hot products such as liquid water. Either such a phase separation is absent or is not significant enough to be observable in our experiments. As a matter of fact, in the numerical works [15, 16], the authors have shown out that the phase separation had no perceptible effect.

In Figure 10, the liquid-oxygen interface starts to get the transcritical appearance before the chamber actually reaches the oxygen-critical pressure. For instance, for $P_r^{O2} = 0.90$, the upstream portion of the dense jet has the transcritical aspect. At the same time, the downstream one still shows subcritical-type atomization, i.e., with ligaments and droplets still being discernible. That is because, for a time period of approximately 1 s, the oxygen is transcritical upstream of the injector, i.e., $P_{O2} > P_c^{O2}$, whereas the chamber is still at subcritical pressure, i.e., $P < P_c^{O2}$. Hence, upon discharging into the combustion chamber, the liquid-oxygen jet progressively relaxes from transcritical to subcritical states. To quantify this transient process, we define a normalized parameter $\Pi_{\%}$ as:

$$\Pi_{\%} = \frac{P_{O2} - P_c^{O2}}{P_{O2} - P} \tag{1}$$

The parameter $\Pi_{\%}$, whose evolution is plotted in Figure 13, has been constructed to represent the progression from a condition whereby critical pressure is attained only upstream of the injector exit plane ($P_{O2} = P_c^{O2}, \Pi_{\%} = 0$) to a condition whereby the whole combustion chamber is at critical pressure ($P = P_c^{O2}, \Pi_{\%} = 1$). Figure 14 provides visualizations of the interface at different values of $\Pi_{\%} \in [0, 1]$. As $\Pi_{\%} \rightarrow 1$, the interface appears to get less corrugated, and the ligaments and droplets have completely disappeared for $\Pi_{\%} = 1$. In Figure 14 and its associated video, we notice a transverse oscillatory motion of the jet. This indicates an unsteady flapping motion, which is further analyzed in §4.2. For $0 < \Pi_{\%} < 1$, liquid-oxygen droplets detaching from the core in the upstream region first transit to the supercritical state through pseudo-boiling to the surrounding hot gases. Then, they transit to the gaseous state. As opposed to this, those detaching in the downstream region first transit into the subcritical state then to the gaseous state through vaporization. This point is schematically represented in Figure 15.

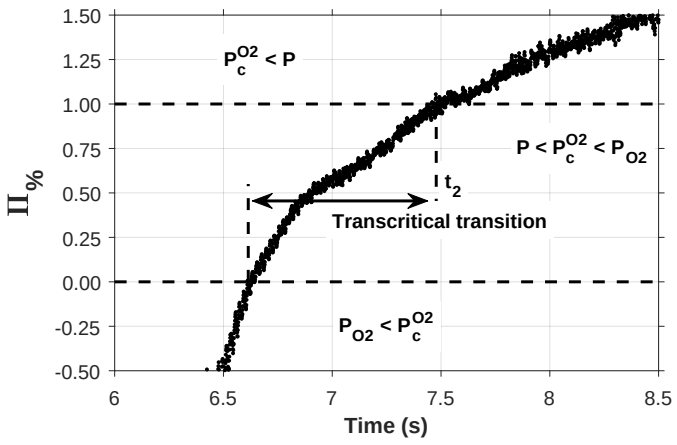

Figure 13: Evolution of the transcritical-transition parameter $\Pi_{\%}$.

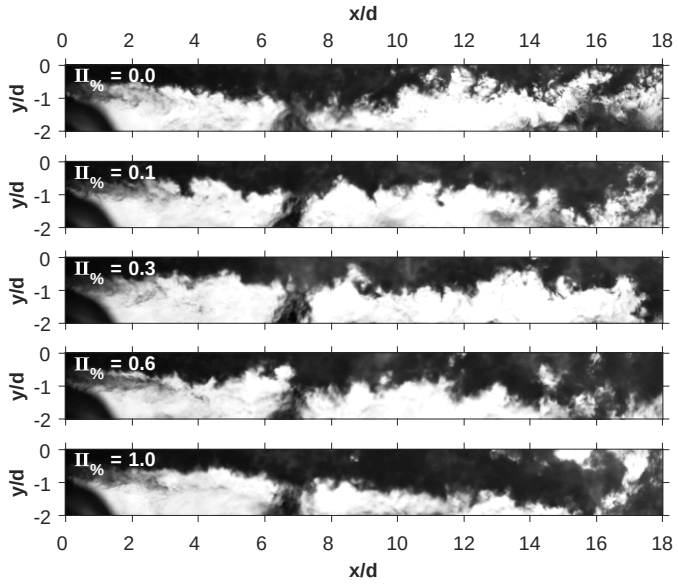

Figure 14: Visualizations of the liquid-oxygen interface at different values of the transcritical-transition parameter $\mathbf{\Pi}_{\%}$.

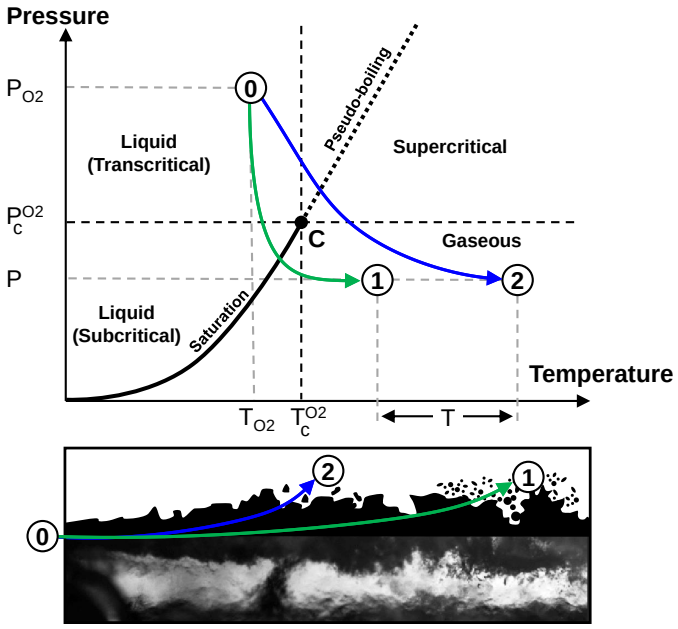

Figure 15: Schematic illustration depicting the possible coexistence of pseudo-boiling and vaporization transitions when $0 < \mathbf{\Pi}_{\%} < 1$. Station ⓪ denotes the thermodynamic state of the oxygen upon entering the combustor. The trajectories ⓪→① and ⓪→② represent the two generic possible-paths the liquid-oxygen droplets can follow. When $\mathbf{\Pi}_{\%} < 0$, the trajectories merge into the generic ⓪→① path. When $\mathbf{\Pi}_{\%} > 1$, the trajectories merge into the generic ⓪→② path.

4. Analysis

4.1. Gaseous Case Low-Frequency instability

A particular phenomenon observed during the Gaseous Case operation is the establishment of a Low-Frequency (LF) instability of the central flame and possibly of the surrounding ones. The instability triggers as soon as the flame anchors at the injector lip and continuously subsists during the pressure ramps and the plateau period. It manifests as a transverse flapping motion of the flame as shown in Figure 16, which provides consecutive OH* chemiluminescence snapshots taken within the stabilized plateau. Because OH* chemiluminescence is a 2D representation of a 3D phenomenon, we could only observe a transverse motion of the flame. Since the geometry is symmetric, we believe this motion could be that of a precession of the flame around the injector axis. In order to better understand the origin of the instability, the Spectral Proper Orthogonal Decomposition (SPOD) technique, in the form developed in [69], is performed on the OH* chemiluminescence recording. Similar to other modal decomposition techniques, SPOD aims at extracting coherent structures embedded within a flow, which *apriori* appears chaotic, e.g., acoustic induced resonance, vortex-shedding-type instabilities. We do not describe here the algebraic details of the technique. Thorough descriptions of modal decomposition methods applied to various fluid dynamics problems and comparisons between techniques could otherwise be found in [69, 70]. Phenomenologically, the SPOD method brings together the advantages of frequency ranking from the Dynamic Mode Decomposition (DMD) and of optimality (in the least-squares sense) from the standard (also termed snapshot or space-only) Proper Orthogonal Decomposition (POD) [69]. Thereby, the SPOD method rules out the disadvantages of both methods, i.e., the non-orthonormality and non-optimality of DMD and the frequency mixing of POD. As such, the SPOD method returns modes representing structures

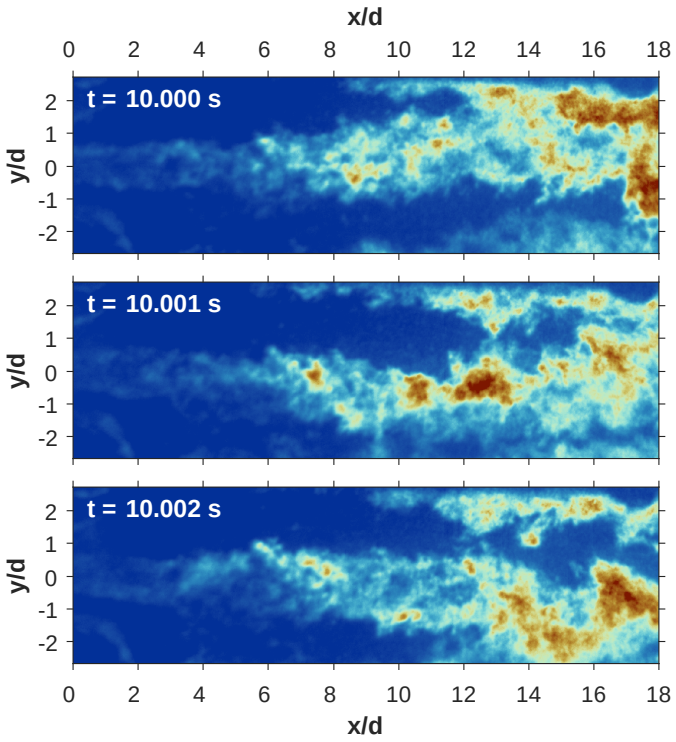

Figure 16: Series of OH* chemiluminescence snapshots recorded during the stabilized plateau of the **Gaseous** Case. The time interval between snapshots is 1 ms.

that evolve coherently both in space and time. The only drawback of the method is that it requires a longer time-realization of the process studied. We have used the open-source Matlab implementation (`spod`) of the SPOD algorithm [71] and applied it on a series of $N_t = 3600$ images taken within the stabilized plateau, i.e., spanning 3.6 s of the recording. Specifically, the spectral estimation parameters of the algorithm [71] are set as follows: $N_{FFT} = 800$ (block length), $N_{ovlp} = N_{FFT}/2 = 400$ (50-percent-overlap), $N_{blck} = (N_t - N_{ovlp})/(N_{FFT} - N_{ovlp}) = 8$ (number of blocks). The resulting frequency resolution is $\Delta f = f_s/N_{FFT} = 1.25$ Hz, with f_s the sampling (recording) frequency. Figure 17 (a) shows the frequency distribution (spectral density) of the most dominant ($m = 1$) SPOD-modes. We observe a frequency peak at $f = 93.75$ Hz. For this frequency, Figure 17 (b) gives the distribution of the energy (the eigenvalues) between modes, normalized by the sum of the eigenvalues at the same frequency. The term energy is used here as an analogy to the space-integral turbulent kinetic energy since this represents the sum of the eigenvalues when SPOD is applied to a velocity fluctuations field [71]. The most dominant mode hence retains 60% of the energetic content at the $f = 93.75$-Hz-frequency. Finally, Figure 17 (c) shows the mode's shape (real part) relative to the retained frequency. It indicates a transverse oscillatory motion which we associate with the flapping or precession instability.

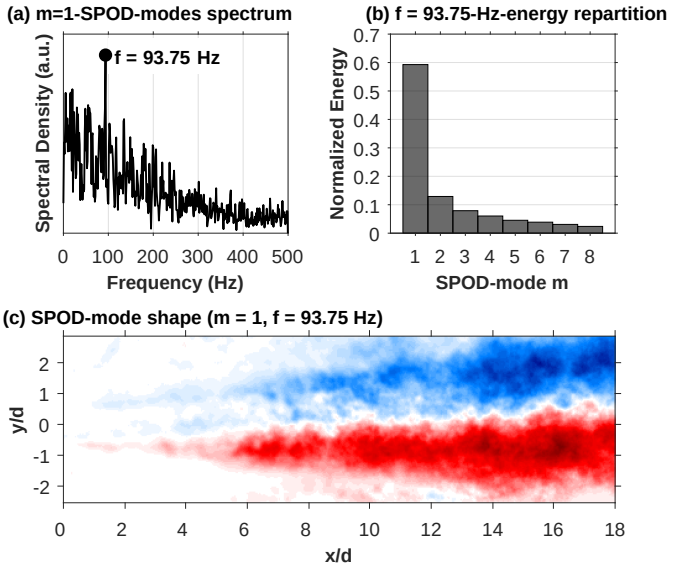

Figure 17: Spectral Proper Orthogonal Decomposition (SPOD) analysis performed on a sequence of OH* chemiluminescence images within the **Gaseous** Case stabilized plateau. **(a)** Spectral Density of the most dominant ($m = 1$) SPOD-modes. **(b)** Normalized Energy distribution at the $f = 93.75$-Hz-frequency. **(c)** Shape of the most dominant SPOD-mode at the $f = 93.75$-Hz-frequency.

At this stage, the flapping instability has been spectrally characterized. Nevertheless, we need to understand its origin. A first explanation originates from the acoustic resonance of the O_2 feed line. On the one hand, Figure 18 shows the FFT of the dynamic pressure recording in the O_2 feed line. The frequency peak found at 96 Hz well coincides with the oscillation frequencies found by the SPOD analysis. Note that the peak-to-peak amplitude of this oscillation is only about 0.7% of the mean pressure. On the other hand, considering that the

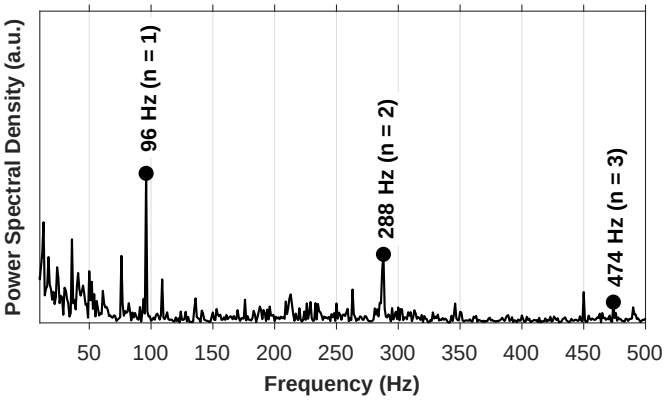

Figure 18: Fast Fourier Transform (FFT) of the oxygen feed line dynamic pressure recorded during the **Gaseous** Case stabilized plateau.

feed line could be modeled as a closed-open cavity between the sonic throat located upstream and the injection plate, the eigenfrequencies of the longitudinal modes are determined according to:

$$f_{nL} = \frac{(2n-1)a_{sound}}{4L_{line}} \tag{2}$$

where a_{sound} is the speed of sound in the medium (uniform O_2 at $T = 290$ K) and L_{line} is the length of the oxygen feed line. This is measured from the position of the upstream sonic throat down to the injection plate. Table 3 provides the values of the first three eigenfrequencies ($n = 1, 2, 3$). These correspond to

	$n = 1$	$n = 2$	$n = 3$
f_{nL} **(Hz)**	94.6	283.7	472.8

Table 3: Theoretical values of the first three ($n = 1, 2, 3$) acoustic eigenfrequencies of the oxygen feed line.

the clear-cut frequency peaks observed in Figure 18, which indicates that the feed line is resonating. It is, however, still unclear how this longitudinal acoustic resonance resulted in a precession or flapping motion in the combustion chamber.

A second explanation is of hydrodynamic nature. Indeed, in [72], the authors have observed a similar instability in a multiple-injectors arrangement using a lean premixed methane-air mixture. The so-called confinement-induced instability is reported to occur at a characteristic Strouhal number $St = 0.012$, albeit they also observed this phenomenon for $0.001 < St < 0.01$ in previous studies. In our case, considering the oxygen nozzle diameter and injection velocity, we find that the instability occurs at a Strouhal number of $St = fd/U_{O2} = 0.008$, which is in agreement with the observations of [72].

4.2. Unsteady dynamics of the liquid-oxygen jet

As mentioned in Section 3.3, the transcritical-oxygen jet also appears to be flapping in an apparent transverse motion. Qualitatively, the spatial extent of the motion is much smaller than that obtained in the Gaseous Case (see §4.1). Again the apparent flapping motion may be that of the precession of the

jet axis around the injector axis. We applied the SPOD technique on the backlit visualizations to extract the coherent structure of the instability. We used the algorithm on a series of ∼ 4000 snapshots within the stabilized plateau of the Transcritical Case. Figure 19 shows some outcomes of the decomposition. On the most dominant mode ($m = 1$) spectrum, we can identify four clear-cut frequencies standing out of the background noise.

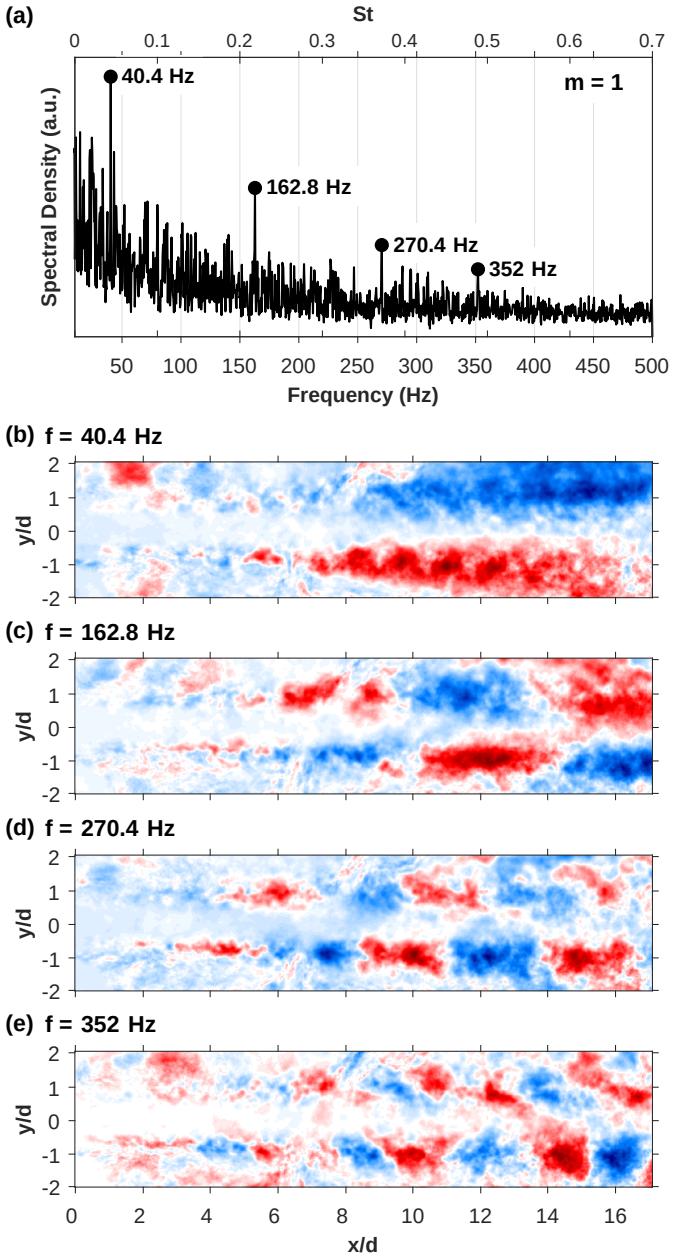

Figure 19: Spectral Proper Orthogonal Decomposition (SPOD) analysis performed on a sequence of backlit images within the **Transcritical** Case stabilized plateau. **(a)** Spectral Density of the most dominant ($m = 1$) SPOD-mode. Note that the top horizontal-axis provides values of the oxygen-injection-based Strouhal number, $\mathbf{St = fd/U_{O2}}$. **(b–e)** Shapes of the most dominant SPOD-mode for the isolated frequencies.

The first frequency, at $f = 40.4$ Hz, has a shape that recalls that obtained for the Gaseous Case flapping instability. As opposed to the Gaseous-Case, whereby the instability occurred at the $f = 93.75$-Hz-frequency and could be linked to a coupling between the 1L acoustic resonance of the oxygen feed line and a confinement-induced instability, the present instability does not seem to be of the same origin. On the one hand, the 1L eigenfrequency of the oxygen feed line is, in the present case, $f \sim 250$ Hz (liquid-oxygen sound velocity is ∼ 2.6 times that of the gaseous oxygen). On the other hand, the oxygen-injection-based Strouhal number of the instability, $\mathrm{St} = fd/U_{O2}$, is here ∼ 0.0513, which is not on the range of the confinement-induced instability reported in [72], i.e., $0.001 < \mathrm{St} < 0.01$. Consequently, the observed instability is instead a self-induced instability of the type encountered in shear-coaxial liquid jet, as those studied in [73].

The three other identified frequencies, namely f =162.8, 270.4 and 352 Hz, respectively associated to Strouhal numbers St = 0.21, 0.34 and 0.45, are all the signature of Kelvin-Helmholtz instabilities developing at the oxygen interface. Recall that, at transcritical pressure, the liquid oxygen behaves somehow like a gas (see §3.3). Their shapes have a wave packet structure with the alternation of blue and red regions in the direction of the jet at both apparent interfaces (top and bottom). They are indeed similar to those observed in previous works where the authors investigated the vortex-shedding phenomenon, e.g., that developing in turbulent jets [69], through modal decomposition techniques. Besides, the measured values of St are in the range $0.2 < \mathrm{St} < 0.6$ of possible vortex-shedding modes [74–76].

In short, the dynamic of the oxygen core contains a flapping instability superimposed to vortex-shedding instabilities of several harmonics. We also performed the SPOD analysis on the Transcritical Case rerun (Transcritical Case 2) recorded at the 15-kHz-frame rate, which gave us access to higher frequency content. The returned modes are essentially the same as no additional modes appeared for $f > 500$ Hz.

We also applied the technique to the backlit recording of the Subcritical Case. On the dominant mode ($m = 1$), we could again identify a coherent space/time structure associated with the liquid jet flapping, albeit of reduced spatial amplitude. Figure 20 compares the dominant mode found to that of the Transcritical Case. The frequency peak is located at $f = 29.6$ Hz, corresponding to a Strouhal number of St = 0.0514, which is very close to that measured for the Transcritical Case (St = 0.0513). This proximity tends to confirm that the liquid jet instability is of a self-induced nature. It seems to occur at a constant Strouhal value and does not appear to depend on the pressure nor on the presence of the flame since it also manifested on the backlit recordings of the non-reactive runs.

4.3. Primary-atomization description

In order to quantitatively describe the primary breakup atomization process, we propose to determine the liquid core length L (also called undisturbed length or intact core length). It is classically defined [62] as the maximum downstream position above which the liquid core starts to fragment into droplets and ligaments, i.e., above which the liquid jet no longer forms a continuous phase. In Figure 21, we illustrate the procedure

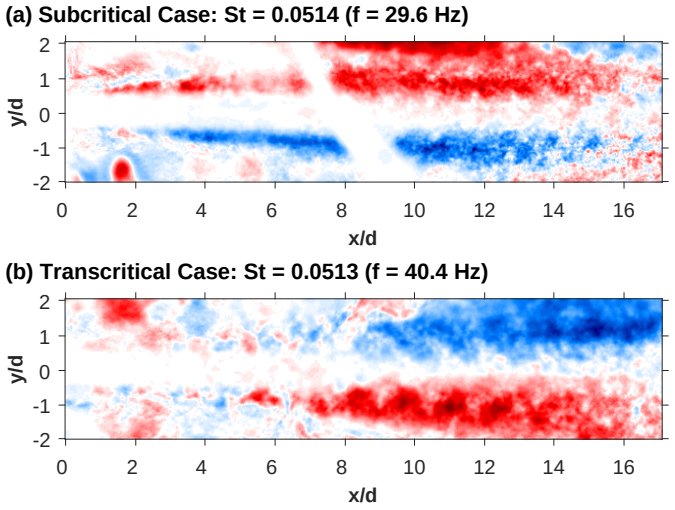

Figure 20: Comparisons of the most dominant space/time mode between the **Subcritical (a)** and **Transcritical (b)** cases.

to extract this length. First, the backlit image is binarized using the Matlab global thresholding algorithm based on Otsu's method [77]. On top of the binarized image, we draw a fan of lines spreading across the spray cone. We then look for the line that maximally and continuously covers the binarized liquid region, and we measure the length L along. For the Subcritical

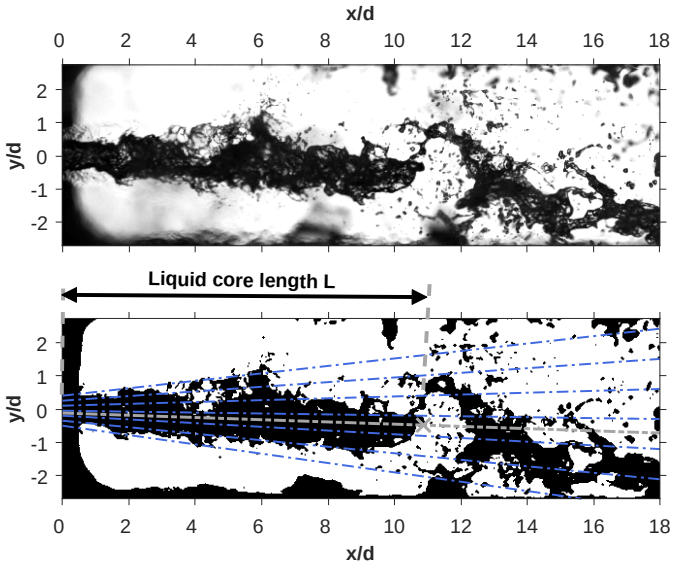

Figure 21: Determination of the liquid core length L. **Top:** instantaneous backlit visualization. **Bottom:** corresponding binarized image.

Case, Figure 22 gives the evolution of L (symbols). The instantaneous measurement constitutes quite a fluctuating signal with amplitudes of oscillation rising to $\sim 30\%$. The oscillation is due to the measurement of L being stochastic in nature [78]. At a given time, the liquid core length can either grow or substantially decrease when the oxygen core, at the tip of which the length is being measured, disintegrates. Consequently, the detected length abruptly drops. In addition, the 3D nature of the atomization, which is being reduced to a 1D-parameter-representation measured in 2D, also explains why the values of L appear to be chaotic. Subsequently, we applied a moving average filter of 0.25-s-width to the measured data (the line in Figure 22). For time $t > 5.5$ s, the complete breakup of the liquid jet intermittently occurs downstream of the visualization window and could therefore not be measured. In Figure 22, we compare the measurements of L to a selection of semi-empirical correlations formulated in the literature for shear-coaxial injectors, namely those of Mayer (1961, reported in [62]), Eroglu et al. [79] and Davis and Chehroudi [80]. Table 4 provides details of each formulation. They all convey the phenomenological idea that the liquid core breakup is governed by the competition between stabilizing parameters (surface tension and inertia forces) and destabilizing ones (aerodynamic friction imposed by the gaseous stream). They were proven to provide satisfactory agreement with experimental results obtained in the Mascotte bench [40]. Still, the comparison was, at that time, based on mean values, obtained on a steady atomizing LO_2/H_2 configuration, not the dynamically evolving configuration of the present work. Also, these correlations are based on cold flow atomization experiments. As such, they may not hold anymore in reacting (hot) conditions since the aerodynamic friction imposed by the gaseous stream is significantly reduced owing to the severe reduction of the gaseous density around the liquid jet. In Figure 22, the measured and correlations-derived values are of the same order magnitude, but their trends differ.

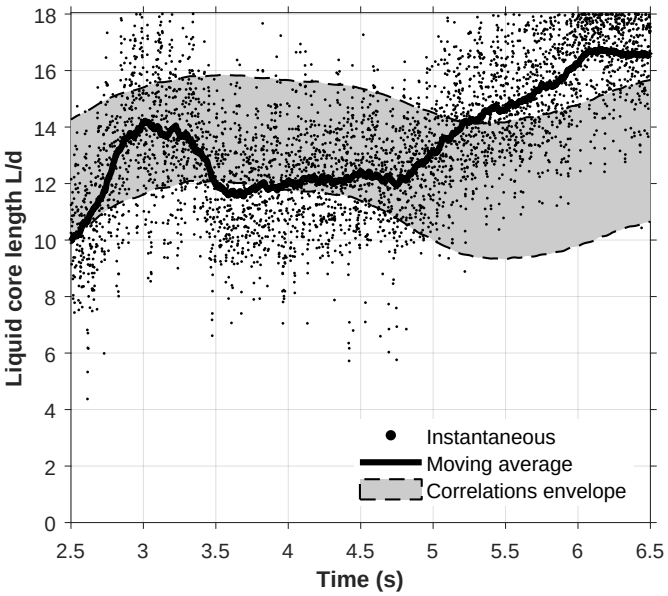

Figure 22: Evolution of the liquid core length L (**Subcritical** Case) compared to that evaluated based on the semi-empirical correlations of Mayer [62], Eroglu et al. [79] and Davis and Chehroudi [80].

Following up on the idea that cold-flow-based correlations no longer holds in reactive conditions, we propose another formulation, which only depends on the inertia imposed to the liquid jet, i.e., its tendency to resist perturbations [29]. That is, L is, on the first order, proportional to the injection velocity (based on the pressure-drop measurement across the injection

Reference	Correlation for L/d
Mayer [62]	$\frac{C_1}{J^{2/3}}\left(\frac{\sigma}{\mu_L U_L}\right)^{1/3}$
Eroglu et al. [79]	$0.66\mathrm{Re}^{0.6}\mathrm{We}_{\Delta U}^{-0.4}$
Davis and Chehroudi [80]	$25J^{-0.2}$

Table 4: Semi-empirical correlations of Mayer [62], Eroglu et al. [79] and Davis and Chehroudi [80] for the determination of the liquid core length of shear-coaxial injectors. $\boldsymbol{C_1}$: adjustable constant, $\boldsymbol{J}$: Momentum Flux Ratio, $\boldsymbol{\sigma}$: liquid surface tension, $\boldsymbol{\mu_L}$: liquid dynamic viscosity, **Re**: Liquid-injection-based Reynolds number, $\mathbf{We}_{\boldsymbol{\Delta U}}$: Weber number based on the gaseous/liquid velocity difference.

plate, $\Delta P_{O2} = P_{O2} - P$):

$$\frac{L}{d} = k\sqrt{\frac{\Delta P_{O2}}{\rho_{O2}}} \tag{3}$$

For each case where L could be experimentally determined, i.e., within the visualization region, we have approached the measurement of L with the correlation (3). Hence, Figure 23 provides the measurement (moving-average filtered) of L and compares it to that estimated by the correlation (3). We consider the two reruns, numbered 1 and 2, of the Subcritical and Transcritical cases. We find that the correlation well reproduces the dynamic evolution of L. The correlation coefficient k is framed to a mean value $k = 0.61$ s/m and with satisfactory accuracy, as a standard deviation $\sigma_k = 0.0216$ s/m (3.5% of the mean) is obtained.

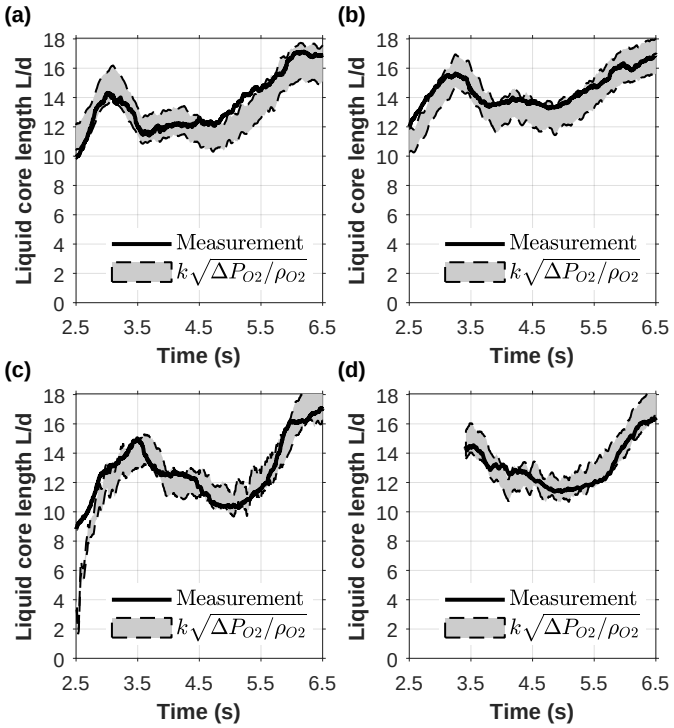

Figure 23: Comparisons between the dynamic measurements of the liquid core length $\boldsymbol{L}$ and the proposed initial inertia-based correlation (3). **(a) Subcritical** Case 1. **(b) Subcritical** Case 2. **(c) Transcritical** Case 1. **(d) Transcritical** Case 2. The shaded areas correspond to the 95% Confidence Interval ($\pm 2\sigma_k$) of the correlation coefficient k.

4.4. Probabilistic description of the spray

For the Transcritical Case 2 (Figure 23 (d)), we observe a time period, between $t = 4.75$ s and $t = 5.5$ s (subcritical pressure), for which L is approximately constant with a time-averaged value of $L_{\mathrm{avg.}}/d = 11.6$. For this time period, we quantitatively characterize the atomization process through a probabilistic description of the spray. To that end, we use the objects detected using the binarization described above. For each detected object, we perform a circularity check in order to decide to count or discard it as a droplet. In addition, we used the gradient-based methodology proposed in [81] to discard out-of-focus objects. This inhibits the detection of the droplets originating from the outer-injectors jets. The backlit-imaging resolution is not sufficient to allow for the whole range of droplet diameter to be detected. The resulting droplet-diameter distributions are hence ill-characterized, i.e., truncated because of the detection limit and biased towards the larger diameters. As such, characteristic diameters, such as the Sauter Mean Diameter, could not be correctly determined. Some 11251 images, between $t = 4.75$ and $t = 5.5$ s, are used to populate the statistical sample. We choose to base the probabilistic description on the Transcritical Case 2 because it benefits from a higher sample size than the other 1-kHz-recordings. About 1.74 million droplets are thereby sampled, i.e., on average $\sim$ 155 droplets are detected at each frame.

Figure 24 provides the fields of the probability of liquid presence P_{LP} and droplet presence P_{DP}. The Probability of Liquid Presence can alternatively be interpreted as the time-averaged liquid volume fraction. A Gaussian filter is applied to the P_{DP} fields to smooth out the noise. White regions are those where liquid or droplets are not detected, or their presence could not be correctly ascertained. Both probability fields are arranged around a bottom-deflected axis of symmetry (x'). This deflection results from the action of gravity, which, for the low-velocity conditions of the time period considered, does have a noticeable effect. The x' axis hence approximates the jet trajectory (parabola). Along this axis, Figure 25 (a) provides the profiles of P_{LP} and P_{DP}. The latter is normalized by its maximum value. Figure 25 (b) shows the profiles sampled along the orthogonal axis y' at the position $x' = L_{\mathrm{avg.}}$. We observe that P_{LP} and P_{DP} are inversely correlated, which is a manifestation of the mass-conservation of the liquid from the continuous to the dispersed phases associated with, respectively, the liquid core and the droplets.

5. Conclusions

In this work, we have presented results of an experimental investigation into the dynamics of a subscale rocket combustor operating with five shear-coaxial injectors fed with methane

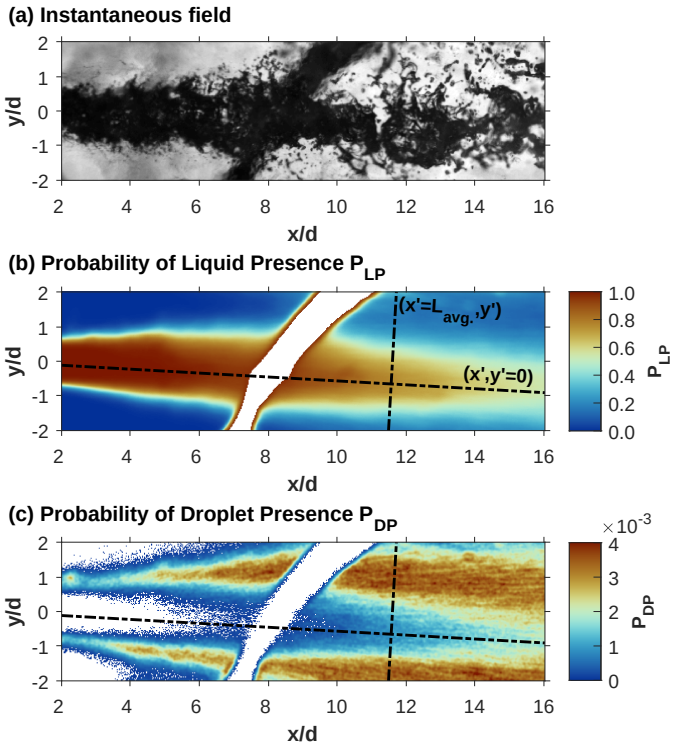

Figure 24: Probabilistic description of the spray for the subcritical time-period of the **Transcritical** Case 2 recorded at 15 kHz. (a) Instantaneous backlit visualization. (b) Probability of Liquid Presence $\boldsymbol{P_{LP}}$. (c) Probability of Droplet Presence $\boldsymbol{P_{DP}}$. On subfigures (b) and (c), white areas correspond to regions where liquid or droplets are not detected, or their presence could not be correctly ascertained. The dotted lines $(x', y' = 0)$ and $(x' = L_{avg.}, y')$ are, respectively, the symmetry axis of both probability fields and its orthogonal axis at the position of the time-averaged breakup. The profiles plotted in Figure 25 are sampled along these two axes.

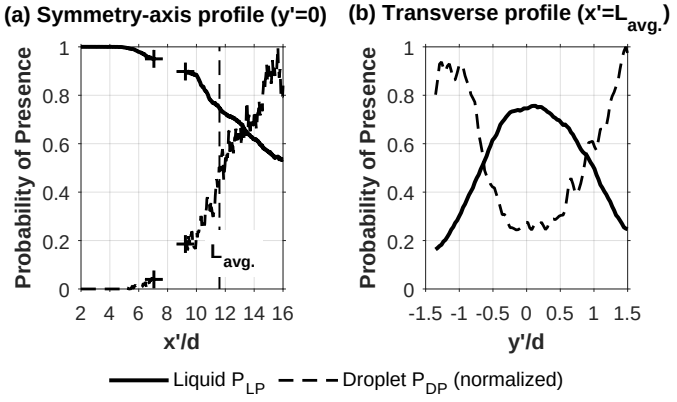

Figure 25: Profiles of $\boldsymbol{P_{LP}}$ and $\boldsymbol{P_{DP}}$ sampled along **(a)** the liquid-jet apparent symmetry axis and **(b)** its orthogonal axis at the position of the time-averaged breakup (see Figure 24). The profiles of P_{DP} are normalized by their respective maximum values. The absence of values between the positions marked with "+" symbols corresponds to the non-measurable region imposed by the visualization-window's crack.

and oxygen. We have described three canonical cases, which we categorized according to the targeted pressure within the combustion chamber relative to the critical pressure of oxygen, namely the Gaseous Case, the Subcritical Case and the Transcritical Case. We simultaneously set OH* chemiluminescence and backlit recordings to visualize the central injector flame and the dynamics of the corresponding liquid jet.

We first provided comparisons between the three canonical cases. In summary, we observed that the OH* chemiluminescence intensity varies almost linearly with the chamber pressure. At the same pressure, we obtained higher OH* intensity between the liquid (subcritical and transcritical) and gaseous cases and between the transcritical and subcritical cases. We understood the first difference as originating from the better mixing of the reactants in gaseous states, which leads to a smaller proportion of the reactants burning around the higher-intensity stoichiometric composition. The second difference is due to the opacification of the visualization window by soot deposit. In future works, additional care will be taken to properly clean the windows of soot deposit.

One of the objectives of this article is to document the transitional dynamics of the flame and liquid-oxygen jet when the combustor pressure exceeds the saturation and critical pressure of the oxygen. As for the former, the oxygen condensation always intervened before the flame had anchored at the injector lip. It would be interesting to observe the case where the flame stabilizes first (with gaseous oxygen injection), and the oxygen condensation follows. Regarding the second transition, backlit recordings provide valuable visualizations of the liquid-oxygen jet progression.

For the Gaseous Case, we observed a Low-Frequency instability on the OH* chemiluminescence recording. The instability manifests as a flapping or precession motion of the flame. We used the SPOD technique to analyze the instability. Note that we have also applied other modal decomposition techniques, i.e., standard POD and exact DMD. They essentially revealed the same dominant mode both spatially and spectrally. Hence, we isolated a structurally-coherent dominant mode of characteristic frequency $\sim$ 95 Hz. We found that this frequency coincides with the 1L acoustic mode eigenfrequency of the oxygen feed line. Alternatively, we observed that the instability well matched the so-called confinement hydrodynamic instability found in previous works [72]. Therefore, it could be the case that the hydrodynamic instability is responsible for amplifying the acoustic resonance in the oxygen feed line or that the acoustic resonance amplifies the hydrodynamic instability. Additionally, hydrodynamic coupling with the surrounding jets could also have a role in the instability. In order to decide which mechanism is at play, we could determine if the instability still manifests for different acoustic-resonant frequencies or Strouhal numbers. Finally, we still need to figure whether we observe the confinement-induced instability if a single-injector is used or in non-reactive conditions. Another open question is whether the flame had a flapping or precession motion. One way to answer this would be to image the combustion chamber either from the front or in two directions orthogonal to the chamber axis or to use the OH-PLIF imaging technique. We should consider a stabilized plateau of pressure $\approx$ 1 MPa for the PLIF-OH technique to be successful. Tiny asymmetrical elements, such as the cavity of the torch located on the top port of the combustor, could otherwise induce the break from symmetry.

Within their respective stabilized plateaux, the Subcritical and Transcritical cases both showed an apparent similar flapping instability (analyzed by means of SPOD), albeit with a much less spatial extent than observed for the Gaseous Case. Unlike the latter, we could not link this instability to any of the aforementioned phenomena, i.e., acoustic resonance or confinement-induced hydrodynamic instability. Instead, we find that they both occur at the same Strouhal number of St ≈ 0.051, which gave us reason to believe that the instability is of self-induced nature. Additional observations for different values of d/U_{O2} would help to confirm this observation. It is worth reminding that none of the described LF instabilities resulted in any noteworthy pressure oscillations in the combustion chamber. It would therefore be compelling to purposefully force an acoustic coupling at the identified Strouhal number.

Finally, we have provided quantitative analyses of the atomization process. First, we dynamically measured the liquid core length. For this, we have proposed a new semi-empirical formulation for its dependency, which is proven better to match the measurement than those of previous works. Second, we provided a probabilistic description of the oxygen spray. The resolution of the backlit images was not sufficient enough to resolve all of the droplet sizes, which resulted in droplet-diameter distributions being truncated and biased. The distributions could be correctly measured by improving the image resolution, as in [8, 82] or through PDI measurements [8].

Acknowledgments

This work was funded by ONERA, the French Aerospace Lab and CNES, the French National Space Agency, through the C3PO (*Combustion Cryotechnique CH4 plus Oxygène*) program. We gratefully acknowledge the technical supports of Éric Paux for the preparation of the test campaign. The preparation and conduct of the Mascotte test facility were made possible by the outstanding contribution of the late Franck Vannier. His technical ability and problem-solving skills will be truly missed. We wish to thank Dr. Zhiyao Yin for the fruitful discussion regarding the analysis of the Low-Frequency instability and its possible connection with the confinement-induced instability phenomenon. We would also like to thank Dr. Robin W. Devillers for proofreading the article and for the valuable suggestions.

Supplementary materials

References

[1] M. Théron, M. Martin Benito, B. Vieille, L. Vingert, N. Fdida, Y. Mauriot, R. Blouquin, C. Seitan, M. Onori, L. Lequette, Experimental and numerical investigation of LOX/Methane Cryogenic Combustion at low mixture ratio, in: 8th European Conference for Aeronautics and Space Sciences (EUCASS), Madrid, Spain, 2019, p. ...

[2] A. Nicole, L. H. Dorey, L. Vingert, M. Théron, LES Simulation For Evaluation Of Acoustic Response Of Subcritical Coaxial Flame Submitted To High-Frequency Acoustic Fields, in: Space Propulsion, Estoril, Portugal, 2021.

[3] G. Singla, P. Scouflaire, C. Rolon, S. Candel, Transcritical oxygen/transcritical or supercritical methane combustion, Proc. Combust. Inst. 30 (2005) 2921–2928.

[4] T. Schmitt, Large-Eddy Simulations of the Mascotte Test Cases Operating at Supercritical Pressure, Flow Turbul. Combust 105 (2020) 159–189.

[5] C. Laurent, G. Staffelbach, F. Nicoud, T. Poinsot, Heat-release dynamics in a doubly-transcritical LO2/LCH4 cryogenic coaxial jet flame subjected to fuel inflow acoustic modulation, Proc. Combust. Inst. 38 (2021) 6375–6383.

[6] S. Candel, M. Juniper, G. Singla, P. Scouflaire, C. Rolon, Structure and dynamics of cryogenic flames at supercritical pressure, Combust. Sci. Technol. 178 (2006) 161–192.

[7] G. Singla, P. Scouflaire, J. C. Rolon, S. Candel, L. Vingert, OH Planar Laser-Induced Fluorescence and Emission Imaging in High Pressure LOx/Methane Flames, J. Propul. Power 23 (2007) 593–602.

[8] N. Fdida, L. Vingert, Y. Mauriot, L. H. Dorey, M. Théron, Comparison of LOx/Methane and LOx/Hydrogen cryogenic spray combustion with simultaneous optical diagnostics, in: 8th European Conference for Aeronautics and Space Sciences (EUCASS), Madrid, Spain, 2019.

[9] F. Richecoeur, P. Scouflaire, S. Ducruix, S. Candel, High-Frequency Transverse Acoustic Coupling in a Multiple-Injector Cryogenic Combustor, J. Propul. Power 22 (2006) 790–799.

[10] Y. Méry, L. Hakim, P. Scouflaire, L. Vingert, S. Ducruix, S. Candel, Experimental investigation of cryogenic flame dynamics under transverse acoustic modulations, C.R. Mec. 341 (2013) 100–109.

[11] L. Vingert, P. Grenard, F. Lévy, A. Nicole, L. H. Dorey, M. Martin Benito, Heat Transfer Measurements in a Water-Cooled Rocket Combustion Chamber Operated with Oxygen/Methane Mixtures at the Mascotte Test Facility, in: 32nd ISTS and 9th NSAT Joint Symposium, Fukui, Japan, 2019.

[12] T. Schmitt, Y. Méry, M. Boileau, S. Candel, Large-Eddy Simulation of oxygen/methane flames under transcritical conditions, Proc. Combust. Inst. 33 (2011) 1383–1390.

[13] N. Guézennec, M. Masquelet, S. Menon, Large Eddy Simulation of Flame-Turbulence Interactions in a LOx-CH4 Shear Coaxial Injector, in: 50th AIAA Aerospace Sciences Meeting, Nashville, TN, USA, 2012.

[14] L. Hakim, T. Schmitt, S. Ducruix, S. Candel, Dynamics of a transcritical coaxial flame under a high-frequency transverse acoustic forcing: Influence of the modulation frequency on the flame response, Combustion and Flame 162 (2015) 3482–3502.

[15] C. Traxinger, J. Zips, M. Pfitzner, Thermodynamic analysis and large-eddy simulations of LOx-CH_4 and LOx-H_2 flames at high pressure, in: Joint Propulsion Conference, Cincinnati, OH, USA, 2018.

[16] C. Traxinger, J. Zips, P. M., Single-Phase Instability in Non-Premixed Flames Under Liquid Rocket Engine Relevant Conditions, J. Propul. Power 35 (2019) 675–689.

[17] Müller, H., Pfitzner, M., Large-eddy simulation of transcritical liquid oxygen/methane jet flames, in: EUCASS Book Series - Advances in AeroSpace Sciences, volume 11, 2019, pp. 177–194.

[18] J. Moore, K. Kuo, Effect of Changing Methane/Oxygen Coaxial Injector Configuration on Diffusion Flame Stability, in: 40th AIAA/ASME/SAE/ASEE Joint Propulsion Conference and Exhibit, Fort Lauderdale, FL, USA, 2004.

[19] C. Pauly, J. Sender, M. Oschwald, Ignition of a gaseous methane/oxygen coaxial jet, in: EUCASS Proceedings Series - Advances in AeroSpace Sciences, volume 1, 2009, pp. 155–170.

[20] M. P. Celano, S. Silvestri, C. Bauer, N. Perakis, G. Schlieben, O. J. Haidn, Comparison of single and multi-injector GOX/CH4 combustion chambers, in: 52nd AIAA/SAE/ASEE Joint Propulsion Conference, Salt Lake City, UT, USA, 2016.

[21] T. Y. Kim, S. Choi, H. K. Kim, I.-S. Jeung, J. Koo, O. C. Kwon, Combustion properties of gaseous CH4/O2 coaxial jet flames in a single-element combustor, Fuel 184 (2016) 28–35.

[22] D. Maestro, B. Cuenot, A. Chemnitz, T. Sattelmayer, C. Roth, O. J. Haidn, Y. Daimon, R. Keller, P. M. Gerlinger, G. Frank, M. Pfitzner, L. Selle, Numerical Investigation of Flow and Combustion in a Single-Element GCH4/GOX Rocket Combustor: Chemistry Modeling and Turbulence-Combustion Interaction, in: 52nd AIAA/SAE/ASEE Joint Propulsion Conference, Salt Lake City, UT, USA, 2016.

[23] S. Silvestri, M. P. Celano, G. Schlieben, O. J. Haidn, Characterization of a Multi-Injector GOX/CH4 Combustion Chamber, in: 52nd

AIAA/SAE/ASEE Joint Propulsion Conference, Salt Lake City, UT, USA, 2016.

[24] M. Shim, K. Noh, W. Yoon, Flame structure of methane/oxygen shear coaxial jet with velocity ratio using high-speed imaging and OH*, CH* chemiluminescence, Acta Astronaut. 147 (2018) 127–132.

[25] J. Wei, M. Ye, S. Zhang, J. Qin, O. J. Haidn, Modeling of a 7-elements GOX/GCH4 combustion chamber using RANS with Eddy-Dissipation Concept model, Aerosp. Sci. Technol. 99 (2020) 105762.

[26] F. Cuoco, B. Yang, C. Bruno, O. J. Haidn, M. Oschwald, Experimental Investigation on LOx/CH4 Ignition, in: 40th AIAA/ASME/SAE/ASEE Joint Propulsion Conference and Exhibit, Fort Lauderdale, FL, USA, 2004.

[27] J. Lux, D. Suslov, M. Bechle, M. Oschwald, O. Haidn, Investigation of Sub- and Supercritical LOx/Methane Injection Using Optical Diagnostics, in: 42nd AIAA/ASME/SAE/ASEE Joint Propulsion Conference and Exhibit, Sacramento, CA, USA, 2006.

[28] D. Salgues, A.-G. Mouis, S.-Y. Lee, D. Kalitan, S. Pal, R. Santoro, Shear and Swirl Coaxial Injector Studies of LOx/GCH4 Rocket Combustion Using Non-Intrusive Laser Diagnostics, in: 44th AIAA Aerospace Sciences Meeting, Reno, NV, USA, 2006.

[29] B. Yang, F. Cuoco, M. Oschwald, Atomization and Flames in LOx/H2- and LOx/CH4- Spray Combustion, J. Propul. Power 23 (2007) 763–771.

[30] B. Yang, F. Cuoco, L. Wang, M. Oschwald, Experimental Investigation of Reactive LOx/GCH4 Coaxial Sprays, in: 43rd AIAA/ASME/SAE/ASEE Joint Propulsion Conference and Exhibit, Cincinnati, OH, USA, 2007.

[31] J. Lux, O. Haidn, Flame Stabilization in High-Pressure Liquid Oxygen/Methane Rocket Engine combustion, J. Propul. Power 25 (2009) 15–23.

[32] J. Martin, W. Armbruster, J. S. Hardi, D. Suslov, M. Oschwald, Experimental Investigation of Self-Excited Combustion Instabilities in a LOx/LNG Rocket Combustor, J. Propul. Power (2021) 1–8.

[33] S. Soller, C. Maeding, B. Kniesner, A. Preuss, N. Rackemann, R. Blasi, Characterisation of a LOx-LCH4 Gas Generator, in: Space Propulsion, Cologne, Germany, 2014.

[34] N. Zong, V. Yang, Near-field flow and flame dynamics of LOx/methane shear-coaxial injector under supercritical conditions, Proc. Combust. Inst. 31 (2007) 2309–2317.

[35] H. Huo, V. Yang, Supercritical LOx/Methane Combustion of a Shear Coaxial Injector, in: 49th AIAA Aerospace Sciences Meeting, Orlando, FL, USA, 2011.

[36] T. Kim, Y. Kim, S.-K. Kim, Effects of pressure and inlet temperature on coaxial gaseous methane/liquid oxygen turbulent jet flame under transcritical conditions, J. Supercrit. Fluids 81 (2013) 164–174.

[37] M. Habiballah, M. Orain, F. Grisch, L. Vingert, P. Gicquel, Experimental studies of high-pressure cryogenic flames on the mascotte facility, Combust. Sci. Technol. 178 (2006) 101–128.

[38] L. Vingert, G. Ordonneau, N. Fdida, P. Grenard, A Rocket Engine under a Magnifying Glass, J. AerospaceLab 11 (2016).

[39] G. Ordonneau, P. Hervat, L. Vingert, S. Petitot, B. Pouffary, First Results of Heat Transfer Measurements in a New Water-Cooled Combustor on the Mascotte Facility, in: 4th European Conference for Aeronautics and Space Sciences (EUCASS), St. Petersburg, Russia, 2011.

[40] N. Fdida, L. Vingert, G. Ordonneau, S. Petitot, Coupling high-speed imaging diagnostics to study a LOX/GH2 flame in a high-pressure rocket combustor, in: 5th European Conference for Aeronautics and Space Sciences (EUCASS), Munich, Germany, 2013.

[41] P. Grenard, N. Fdida, L. Vingert, L. H. Dorey, L. Selle, J. Pichillou, Experimental Investigation of Heat Transfer in a Subscale Liquid Rocket Engine, J. Propul. Power 35 (2019) 544–551.

[42] L. Potier, Large Eddy Simulation of the combustion and heat transfer in sub-critical rocket engines, Ph.D. thesis, Université de Toulouse, 2018.

[43] M. Juniper, A. Tripathi, P. Scouflaire, J.-C. Rolon, S. Candel, Structure of cryogenic flames at elevated pressures, Proc. Combust. Inst. 28 (2000) 1103–1109.

[44] J. Smith, D. Suslov, M. Oschwald, O. Haidn, M. Bechle, High Pressure LOx/H2 Combustion and Flame Dynamics, in: 40th AIAA/ASME/SAE/ASEE Joint Propulsion Conference and Exhibit, Fort Lauderdale, FL, USA, 2004.

[45] J. S. Hardi, H. C. G. Martinez, M. Oschwald, B. B. Dally, LOx Jet Atomization Under Transverse Acoustic Oscillations, J. Propul. Power 30 (2014) 337–349.

[46] J. S. Hardi, S. K. Beinke, M. Oschwald, B. B. Dally, Coupling of Cryogenic Oxygen–Hydrogen Flames to Longitudinal and Transverse Acoustic Instabilities, J. Propul. Power 30 (2014) 991–1004.

[47] G. Herding, R. Snyder, P. Scouflaire, C. Rolon, S. Candel, Flame stabilization in cryogenic propellant combustion, Proc. Combust. Inst. 26 (1996) 2041–2047.

[48] S. Ray, G. Herding, J.-C. Rolon, S. Candel, Analysis of Flame Patterns in Cryogenic Propellant Combustion, Combust. Sci. Technol. 124 (1997) 331–370.

[49] S. Candel, G. Herding, R. Synder, P. Scouflaire, C. Rolon, L. Vingert, M. Habiballah, F. Grisch, M. Pealat, P. Bouchardy, D. Stepowski, A. Cessou, P. Colin, Experimental Investigation of Shear Coaxial Cryogenic Jet Flames, J. Propul. Power 14 (1998) 826–834.

[50] W. Mayer, H. Tamura, Propellant Injection in a Liquid Oxygen/Gaseous Hydrogen Rocket Engine, J. Propul. Power 12 (1996) 1137–1147.

[51] W. O. H. Mayer, A. H. A. Schik, B. Vielle, C. Chauveau, I. Gokalp, D. G. Talley, R. D. Woodward, Atomization and Breakup of Cryogenic Propellants Under High-Pressure Subcritical and Supercritical Conditions, J. Propul. Power 14 (1998) 835–842.

[52] W. Mayer, A. Schik, M. Schäffler, H. Tamura, Injection and Mixing Processes in High-Pressure Liquid Oxygen/Gaseous Hydrogen Rocket Combustors, J. Propul. Power 16 (2000) 823–828.

[53] G. Dieke, H. Crosswhite, The ultraviolet bands of oh fundamental data, J. Quant. Spectrosc. Radiat. Transfer 2 (1962) 97–199.

[54] M. Lauer, M. Zellhuber, T. Sattelmayer, C. J. Aul, Determination of the Heat Release Distribution in Turbulent Flames by a Model Based Correction of OH* Chemiluminescence, in: Turbo Expo: Power for Land, Sea, and Air. Volume 2: Combustion, Fuels and Emissions, Parts A and B, Vancouver, Canada, 2011, pp. 105–115.

[55] L. C. Haber, U. Vandsburger, W. R. Saunders, V. K. Khanna, An Examination of the Relationship Between Chemiluminescent Light Emissions and Heat Release Rate Under Non-Adiabatic Conditions, in: Turbo Expo: Power for Land, Sea, and Air. Volume 2: Combustion, Fuels and Emissions, Parts A and B, Munich, Germany, 2000.

[56] S. Sardeshmukh, M. Bedard, W. Anderson, The use of OH* and CH* as heat release markers in combustion dynamics, Int. J. Spray Combust. Dyn. 9 (2017) 409–423.

[57] L. He, Q. Guo, Y. Gong, F. Wang, G. Yu, Investigation of OH* chemiluminescence and heat release in laminar methane–oxygen co-flow diffusion flames, Combust. Flame 201 (2019) 12–22.

[58] D. Banuti, M. Raju, P. C. Ma, M. Ihme, J.-P. Hickey, Seven questions about supercritical fluids - towards a new fluid state diagram, in: 55th AIAA Aerospace Sciences Meeting, Grapevine, TX, USA, 2017.

[59] D.-Y. Peng, D. B. Robinson, A New Two-Constant Equation of State, Ind. Eng. Chem. Res. 15 (1976) 59–64.

[60] Z. Farago, N. Chigier, Morphological classification of disintegration of round liquid jets in a coaxial air stream, Atomization Sprays 2 (1992) 137–153.

[61] E. J. Hopfinger, Liquid Jet Instability and Atomization in a Coaxial Gas Stream, in: Advances in Turbulence VII, Saint-Jean-Cap-Ferrat, France, 1998, pp. 69–78.

[62] J. C. Lasheras, E. J. Hopfinger, Liquid Jet Instability and Atomization in a Coaxial Gas stream, Annu. Rev. Fluid Mech. 32 (2000) 275–308.

[63] P. J. Linstrom, W. G. Mallard, The nist chemistry webbook: A chemical data resource on the internet, Journal of Chemical & Engineering Data 46 (2001) 1059–1063.

[64] N. Fdida, Y. Mauriot, L. Vingert, A. Ristori, M. Théron, Characterizing primary atomization of cryogenic LOX/Nitrogen and lox/helium sprays by visualizations coupled to phase doppler interferometry, Acta Astronaut. 164 (2019) 458–465.

[65] V. Schmidt, J. Sender, M. Oschwald, Simultaneous observation of liquid phase distribution and flame front evolution during the ignition transient of a LOx/GH2-combustor, J. Visualization 4 (2001) 365–372.

[66] O. Gurliat, V. Schmidt, O. Haidn, M. Oschwald, Ignition of cryogenic H2/Lox sprays, Aerosp. Sci. Technol. 7 (2003) 517–531.

[67] I. H. Bell, J. Wronski, S. Quoilin, V. Lemort, Pure and pseudo-pure fluid thermophysical property evaluation and the open-source thermophysical property library coolprop, Ind. Eng. Chem. Res. 53 (2014) 2498–2508.

[68] O. Kunz, W. Wagner, The gerg-2008 wide-range equation of state for natural gases and other mixtures: An expansion of gerg-2004, J. Chem. Eng. Data 57 (2012) 3032–3091.

[69] A. Towne, O. T. Schmidt, T. Colonius, Spectral proper orthogonal decomposition and its relationship to dynamic mode decomposition and resolvent analysis, J. Fluid Mech. 847 (2018) 821–867.
[70] K. Taira, S. L. Brunton, S. T. M. Dawson, C. W. Rowley, T. Colonius, B. J. McKeon, O. T. Schmidt, S. Gordeyev, V. Theofilis, L. S. Ukeiley, Modal Analysis of Fluid Flows: An Overview, AIAA Journal 55 (2017) 4013–4041.
[71] O. T. Schmidt, T. Colonius, Guide to Spectral Proper Orthogonal Decomposition, AIAA Journal 58 (2020) 1023–1033.
[72] Z. Yin, P. Kutne, I. Boxx, W. Meier, Jet-oscillation-induced combustion dynamics in a multi-nozzle flox® combustor, in: Proceedings of the ASME Turbo Expo 2018: Turbomachinery Technical Conference and Exposition. Volume 4A: Combustion, Fuels, and Emissions. Oslo, Norway, 2018.
[73] A. Delon, A. Cartellier, J.-P. Matas, Flapping instability of a liquid jet, Phys. Rev. Fluids 3 (2018) 043901.
[74] S. C. Crow, F. H. Champagne, Orderly structure in jet turbulence, J. Fluid Mech. 48 (1971) 547–591.
[75] E. Gutmark, C. Ho, Preferred modes and the spreading rates of jets, Phys. Fluids 26 (1983) 2932–2938.
[76] K. Schadow, E. Gutmark, Combustion instability related to vortex shedding in dump combustors and their passive control, Prog. Energy Combust. Sci. 18 (1992) 117–132.
[77] N. Otsu, A Threshold Selection Method from Gray-Level Histograms, IEEE Transactions on Systems, Man, and Cybernetics 9 (1979) 62–66.
[78] J. Locke, S. Pal, R. Woodward, R. Santoro, High Speed Visualization of LOx/GH2 Rocket Injector Flowfield: Hot-Fire and Cold-Flow Experiments, in: 46th AIAA/ASME/SAE/ASEE Joint Propulsion Conference and Exhibit, Nashville, TN, USA, 2010.
[79] H. Eroglu, N. Chigier, Z. Farago, Coaxial atomizer liquid intact lengths, Phys. Fluids A 3 (1991) 303–308.
[80] D. W. Davis, B. Chehroudi, Measurements in an Acoustically Driven Coaxial Jet under Sub-, Near-, and Supercritical Conditions, J. Propul. Power 23 (2007) 364–374.
[81] P. Marmottant, E. Villermaux, On spray formation, J. Fluid Mech. 498 (2004) 73–111.
[82] N. Fdida, L. Vingert, A. Ristori, Y. L. Sant, Droplet size and velocity measurements in a cryogenic jet flame of a rocket-type combustor using high-speed imaging, Atomization Sprays 26 (2016) 411–438.